Rapid basal channel growth beneath Greenland's longest floating ice shelf

Ash Narkevic[1], Beata Csatho[1], and Anton Schenk[1]

[1]University at Buffalo

February 20, 2023

Abstract

Nioghalvfjerdsfjorden Glacier (N79) is one of the two main outlets for Greenland's largest ice stream, the Northeast Greenland Ice Stream (NEGIS), and is the more stable of the two, with no calving front retreat expected in the near future. Using a novel elevation reconstruction approach combining digital elevation models (DEMs) and laser altimetry, previously undetected local phenomena are identified complicating this assessment. N79 is found to have a complex network of basal channels that were largely stable between 1978 and 2012. Since then, an along-flow central basal channel has been growing rapidly, likely due to increased runoff and ocean temperatures, and possibly threatening to decouple the glacier's northwestern and southeastern halves.

Rapid basal channel growth beneath Greenland's longest floating ice shelf

Ash Narkevic[1]**, Bea Csatho**[1]**, Toni Schenk**[1]

[1]Department of Geological Sciences, University at Buffalo, Buffalo, NY, USA.

Corresponding author: A. Narkevic, davidnar@buffalo.edu

Abstract

Nioghalvfjerdsfjorden Glacier (N79) is one of the two main outlets for Greenland's largest ice stream, the Northeast Greenland Ice Stream (NEGIS), and is the more stable of the two, with no calving front retreat expected in the near future. Using a novel elevation reconstruction approach combining digital elevation models (DEMs) and laser altimetry, previously undetected local phenomena are identified complicating this assessment. N79 is found to have a complex network of basal channels that were largely stable between 1978 and 2012. Since then, an along-flow central basal channel has been growing rapidly, likely due to increased runoff and ocean temperatures, and possibly threatening to decouple the glacier's northwestern and southeastern halves.

1 Introduction

The Northeast Greenland Ice Stream (NEGIS) is the largest ice stream of the Greenland Ice Sheet, draining approximately 12% of its surface area and containing a sea-level rise equivalent of 1.1 m (Mouginot et al., 2015). Its discharge is routed through two major outlet glaciers, Zachariæ Isstrøm (ZI) and Nioghalvfjerdsfjorden Glacier (N79) (Fig. 1), the former of which has demonstrated a pattern of accelerating mass loss in recent decades (Mouginot et al., 2019a). N79 features a ∼70 km long floating ice tongue which provides a substantial buttressing effect to this branch of the ice stream (Mayer et al., 2018). At the end of its containing fjord, the ice tongue terminates upon a sill (Morlighem et al., 2017; An et al., 2021).

N79 experienced only minor changes in calving front and grounding line position between 1978 and 2020 (Fig. 1A, Supporting Information Fig. S1), possibly as a result of this configuration. Moreover, models such as the Ice Sheet Systems Model (ISSM) suggest that its grounding line and calving front are unlikely to change significantly over the next century (Choi et al., 2017). However, cosmogenic exposure and radiocarbon dating of surrounding rocks indicate that both N79 and ZI have retreated well inland from their current extents during the Holocene (Larsen et al., 2018), indicating that N79 may be more sensitive to climate change than previously thought. Indeed, velocity measurements show that, while not as dramatically as ZI, N79 has accelerated noticeably in the vicinity of its grounding line (∼ 10%) in recent decades (Mouginot et al., 2015). Moreover, the average water temperature is increasing, and the depth to the upper interface of warm Atlantic Intermediate Water (AIW) is decreasing in the open sea beyond the calving front (Schaffer et al., 2020); and many other glaciers in northern Greenland saw an onset of widespread calving events over the last decade (Ochwat et al., 2022). More recently, evidence of warm AIW has even been found in a marginal surface lake near the N79 grounding line (Bentley et al., 2022).

Laser altimetry time series indicate a dynamic thinning of less than 0.5 m annually between 1999 and 2009 on N79 (Csatho et al., 2014), with longer time series revealing an increased rate of thinning since 2012, with total thinning reaching over 50 m by 2020 close to the grounding line near the center of the glacier (Narkevic et al., 2020). However, this is only observed in a few locations because the sparse spatial coverage of airborne laser altimetry between 2009-2018 (Supporting Information Fig. S2) obscured whether the effect was a minor localized phenomenon or a more widespread trend that largely evaded the available altimetry flight lines. This question has significant implications, as reconstructions based on altimetry (e.g., Khan et al., 2022) make broad conclusions about N79 and other glaciers based on these sparse data.

This uncertainty can be mitigated by including digital elevation models (DEMs), which have a much denser spatial distribution of elevation data, albeit at the cost of poorer precision than altimetry. Using altimetry as control data for correcting any systematic error present in DEMs from multiple years within the time frame of interest can produce a reconstruction with high spatiotemporal resolution and accuracy. Here we present a novel elevation reconstruction of the N79 grounding region using such a technique.

2 Methods

Repeat coverage of WorldView (WV) stereo satellite imagery since 2011 enables the determination of ice sheet elevation changes with high spatial resolution and accuracy (Porter et al., 2022; Shean et al., 2019). We used ArcticDEM strips, generated from WV images using the Surface Extraction with TIN-based Search-space Minimization (SETSM) approach (Noh & Howat, 2018), to reconstruct elevation changes in the N79 region between 2012-2020. These DEMs, calculated using satellite ephemeris information only without applying ground control, still have vertical errors on the order of 4 m (Porter et al., 2022), which is unsuitable for precise change detection and investigating ice dynamic processes of outlet glaciers. We developed a correction algorithm, based on the approach of Schenk et al. (2014) to reduce this error. Altimetry time series, serving as control, were generated from Operation IceBridge Airborne Topographic Mapper (ATM) airborne (1993-2019), ICESat (2003-2009) and ICESat-2 (2018-present) satellite data using the Surface Elevation Reconstruction and Change Detection (SERAC) method (Schenk & Csatho, 2012). A spline-based approximation algorithm (Shekhar et al., 2021) infers the elevation at the date of the DEM acquisition for each time series, and a third-order polynomial correction surface is fitted to the resulting residuals for a given DEM. Once added to the DEM, the error is reduced, and separate DEMs can be mosaicked together with minimal edge discontinuity and a final uncertainty on the order of $\sim$1 m (Supporting Information Text S1). The pipeline also accounts for tidal flexure and the inverse barometric effect on floating ice (Supporting Information Text S2). In this manner, ice surface elevation DEMs, covering the N79 grounding line region, are created for 2012, 2014-2017, and 2020, with nominal dates in the spring to early summer (Supporting Information Table S1). The Greenland Ice Mapping Project (Howat et al., 2014) surface DEM is used outside the spatial extent of the corrected DEMs. A DEM generated from 1978 stereo aerial photographs (Korsgaard et al., 2016) is used for determining long-term elevation changes. Landsat and Sentinel imagery is used for qualitative assessment of surface features (e.g., Supporting Information Table S2).

The 2012-2020 gridded surface elevation reconstructions form the basis of several other data sets. Eulerian (static reference frame) annual elevation change is calculated as the direct difference between surface heights for consecutive years. Furthermore, using a hydrostatic assumption and a bathymetry model from An et al. (2021) as the bed elevation, the depth to the bottom of the ice shelf was inferred for each year and also used for estimating grounding line location (Supporting Information Text S3). The accuracy of the derived ice bottom elevations is assessed by comparing them with airborne ice-penetrating radar (IPR) returns (CReSIS, 2020). Basal drainage patterns are inferred for each year from the surface and bed DEMs using the MatLab Topo Toolbox (Schwanghart & Nikolaus, 2010), and tested for robustness using a Monte Carlo analysis as described in Narkevic (2021). Using this reconstructed basal routing to demarcate a basal drainage basin for N79, annual aggregate runoff is estimated using values from the Regional Atmospheric Climate Model v2.3p2 (van Wessem et al., 2018), assuming all runoff reaches the bed immediately.

Velocities for the period of interest, derived from a combination of radar and optical images using feature tracking and interferometry, are from Mouginot et al. (2019b). These are summer-to-spring annual averages from 2012-2017. From these, the surface strain rate components are derived and used as a proxy for surface stresses, and have an estimated uncertainty of $\sim$0.01 yr^{-1} based on the uncertainty in velocity. Eulerian change rates on floating ice are complicated by the advection of large fractures, so the velocities are used to reconstruct Lagrangian (moving reference frame) elevation changes for this region, i.e., taking the difference between elevation at an initial pixel, and the pixel to which that ice parcel would have advected by the subsequent DEM date (Supporting Information Text S4). This is performed in the manner of Shean et al. (2019).

Finally, to investigate the propagation of dynamic thinning to the grounded ice, SERAC time series derived from altimetry were partitioned into components due to surface processes as estimated by the IMAU-FDM v1.2G model (Brils et al., 2022) and ice dynamics.

3 Results

The cause of the anomalous rapid thinning detected by some SERAC time series is immediately apparent when comparing reconstructions from different years: a large along-flow channel appears in the center of the ice shelf near the grounding line, which experiences a higher rate of thinning than the surrounding ice (Fig. 1B and D-F). Moreover, it is not a novel feature of the ice, but part of an existing pattern of channels that has become increasingly exaggerated over time.

3.1 Morphology of N79

The floating ice shelf of N79 exhibits a lateral dichotomy. The northwestern ice shelf (NWIS) gradually becomes thinner with distance from the grounding line and is marked by a relatively uniform pattern of crevasses, while the southeastern ice shelf (SEIS) is characterized by larger, sparser flow-perpendicular channels separated by $\sim$5-10 km with surface bulges in between (Figs. 1B, 2A) The bulges create an across-flow step-wise thickness discontinuity up to $\sim$100 m at the center of the floating tongue (Reeh et al., 2000, Fig. 1C). This pattern remains visible within $\sim$40 km of the grounding line, beyond which the two halves appear more uniform. There are also three major along-flow channels, one at each margin, and one in the center. The central channel is less uniform than the others, consisting of segments trailing upstream from the northwest end of the SEIS flow-perpendicular channels. Around 2000, a second band of channels with a more oblique orientation appeared closer to the margin, essentially on top of the SEIS marginal channel (Fig. 1B yellow features), one of which causes the southern channel to fork (i.e., Figs. 1C, 1E). Overall, between 1978 and 2020, the ice sheet has become thinner, with more intense and complex channelization, with several channels reaching the grounding line by 2020 (Figs. 1D-F, Supporting Information Figs. S1B, S5).

The flow-perpendicular channels in SEIS are not necessarily analogous to the crevasses in NWIS. Near the grounding line, one can observe annual "ripples" in the ice sheet that first appear angled upstream toward the center and are reminiscent of the basal channel pattern predicted for hetereogenous ice tongues under no-slip conditions by Sergienko (2013), and may represent the nascent form of the large flow-perpendicular channels. These generally rotate until perpendicular to flow, and some ultimately grow a new segment of the central channel, forming a hook shape, and developing a complex surface morphology with internal ridges (Fig. 2B). If in hydrostatic equilibrium, these ridges would correspond to subglacial keels, or they may be uncompensated compressional features. There are no radar flights spanning the flow-perpendicular channels to indicate which is the case. Over time (i.e., with distance from the grounding line), the flow-perpendicular channels tend to become narrower along-flow and more subdued in vertical relief.

Around 2012, two flow-perpendicular channels emerged near the grounding line in close proximity, the second of which did not fully rotate into flow-perpendicular position in subsequent years (Fig. 1B). The central channel segment connected to this flow-perpendicular channel has since grown, thinning the ice in its location at a prodigious rate, reaching nearly 100 myr^{-1} between 2017-2020 at the intersection of the transects in Figs. 2C-2D. This thinning is nearly twice the 50 myr^{-1} melt rate detected in 2011-2015 near the grounding line (Wilson et al., 2017). SERAC time series indicate the ef-

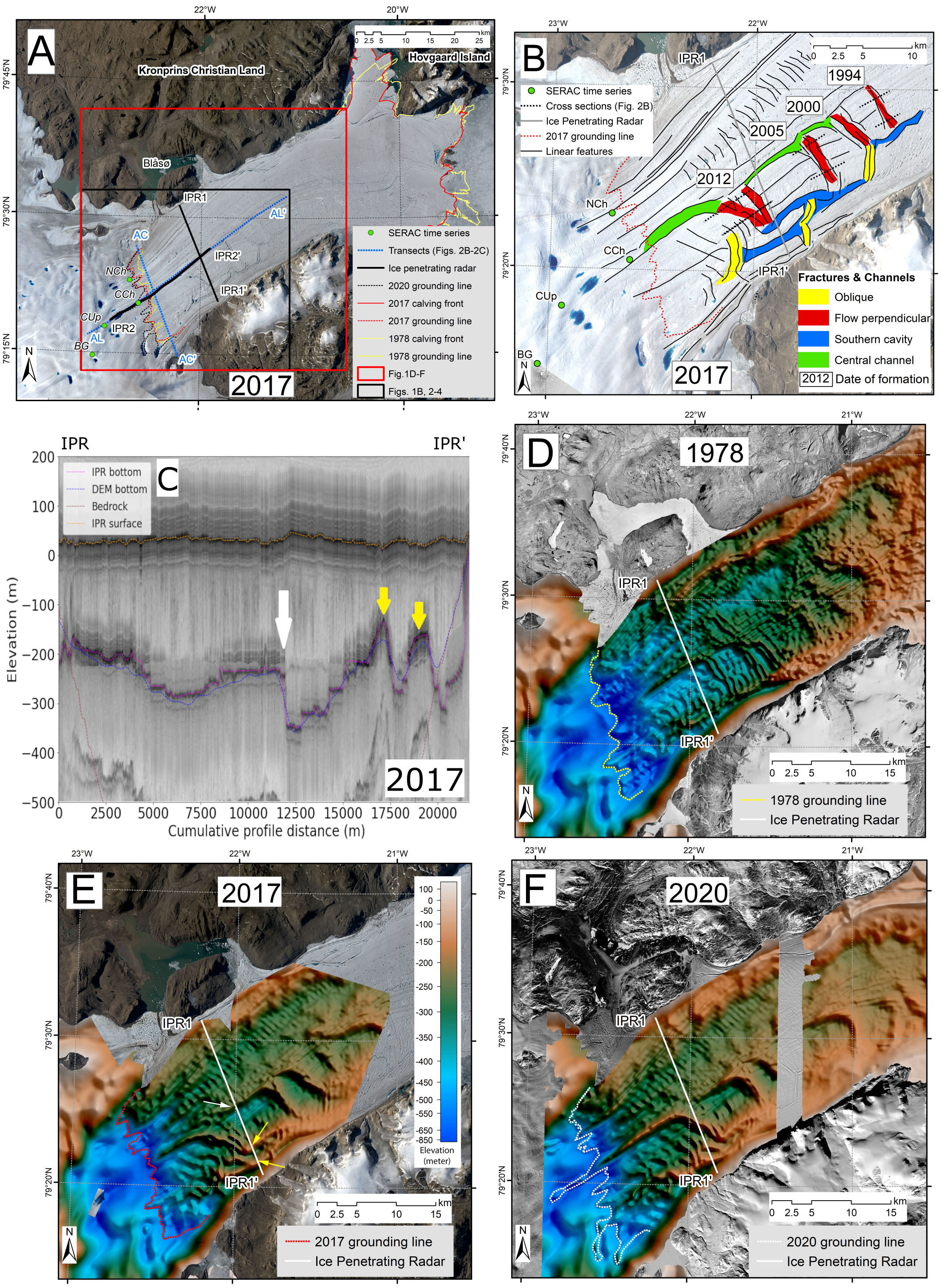

Figure 1. (A) Map of the study area showing calving-front and grounding-line changes between 1978 and 2020, and the locations of transects and SERAC times series. The larger box marks the area shown in Figs. 1D-1E, and the smaller box in Figs. 1B, 2-4, and Supporting Information Figs. S5-7. (B) Interpretation of observable surface features, with the year of formation for flow-perpendicular channels. (C) IPR profile from April 3, 2017, showing the abrupt flow-perpendicular thickness change across the center (white arrow) and the (forked) southeast marginal channel (yellow arrows, see arrows also in Fig. 1E). (D) 1978 ice bottom reconstruction, showing the buoyancy-inferred bottom depth for floating ice, and bedrock depth elsewhere. (E, F) Similar reconstructions for 2017 and 2020. Satellite images and aerial photographs shown in the figures are listed in Supporting Information Table S2.

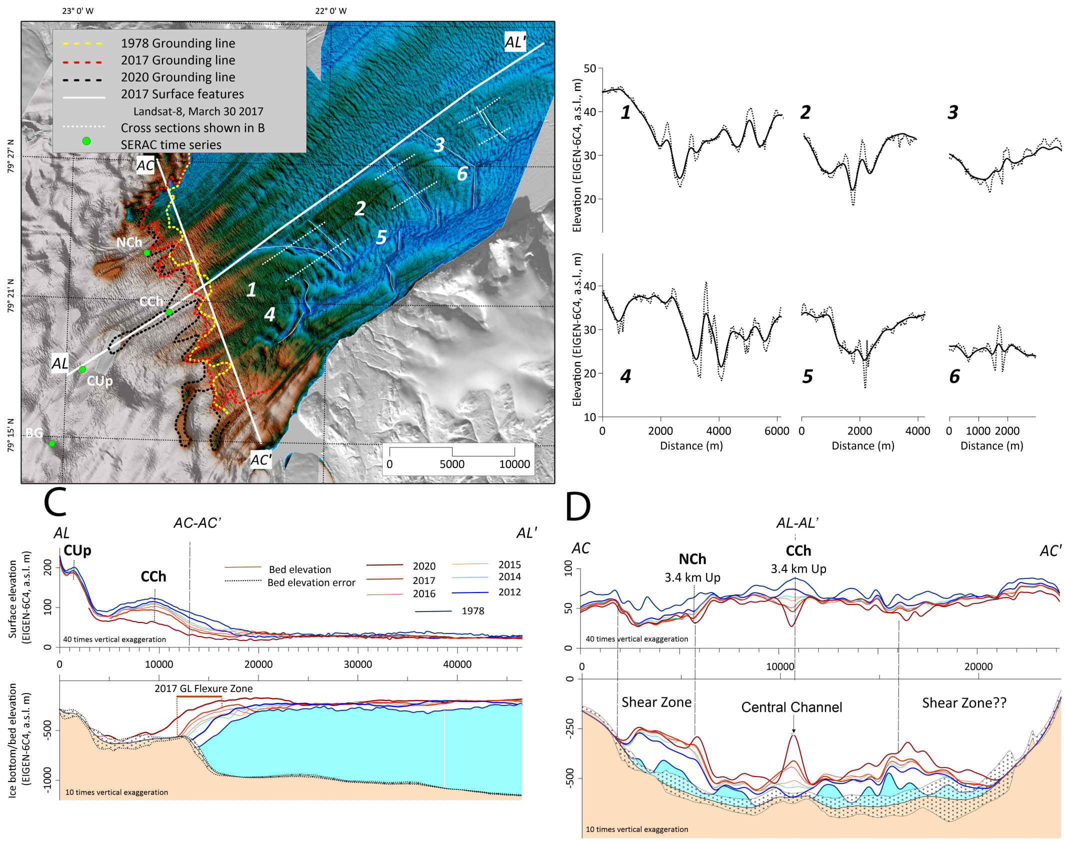

Figure 2. (A) Shaded relief ice surface elevation in 2017 with grounding line locations, ice shelf fractures from Landsat imagery, and locations of transects shown B. (B) Surface elevation profiles across flow-perpendicular channels, illustrating their complex morphology. Dotted lines show elevations from the 30-meter resolution DEM and solid lines from the DEM smoothed by a Gaussian kernel of 600 meter to emphasize surface topography reflecting basal channels. (C) Along and (D) Across-flow profiles of ice surface and bottom elevation showing central channel growth (C, D), grounding line retreat (C), and thinning in the shear zones (D). Shear zone extent is defined based on across-flow strain rates (Fig. 4B) and 2017 grounding line flexure zone is from (ESA, 2017)

fects were already detectable upstream of the grounding line by ∼2015 (Fig. 3F). Thinning continued along the basal channel and the connected subglacial channel (Figs. 3F, S6), and by 2020 the hydrostatically-inferred grounding line had experienced significant local retreat upstream of the central and SEIS marginal channels (Figs. 2A, 2C). This effect was sufficiently pronounced to shift the basal drainage patterns in the area. The potential basal drainage pathways from the reconstruction indicate three major outlets into the fjord: two corresponding to the marginal channels and one that, before 2016, entered the fjord about 1 km southeast of the central channel. By 2016 the channelized thinning shifted this pathway directly into the central channel (Fig. 3A, Supporting Information Fig. S5). The ensuing inferred grounding line retreat then proceeded along the central and southern basal drainage paths. These results, however, come with the caveat that the bed elevation in this area is uncertain and cannot be strongly claimed without additional evidence described below.

While there are no radar flights over the basal channel-subglacial channel system, inferences supporting its rapid thinning and corresponding grounding line retreat can be made from the 2014 and 2017 along-flow IPR transects, which are slightly southeast of and parallel to the channel (Fig. 3B-C). In the grounding zone (7500 to 13000 m along-track) one can see that the ice bottom horizon by 2017 has become both more reflective, indicating there is more water, and slightly higher. This suggests the area was grounded in 2014, and not fully grounded three years later. The ice bottom derived from surface elevation assuming hydrostatic equilibrium underestimates the bottom of the floating ice (Fig. 3C), suggesting that the ice is not in hydrostatic equilibrium. The 2017 radar profile also depicts the rapidly thinning ice shelf basal channel as a new "ghost" horizon ∼200 m above the ice bottom picks, which is likely a side echo from the bottom of the basal channel, about 100 m higher than it was in 2014 (Fig. 3B, 3C). One can also see the expression of the basal channel at the point where the flight crosses the hook-shaped connection between the central and 2012 flow-perpendicular channels, and it is even thinner than in the surface DEM-based reconstruction. Finally, the flattening of the ice sheet surface "bump" along the basal channel by 2020 (Fig. 2C, around CCh) also suggests the transition from grounded ice to floating ice conditions.

The increasing dynamic thinning of the grounded ice is illustrated by the SERAC elevation time series reconstructions shown in Fig. 3F. About 2.5 km upstream of the 2015-2017 grounding line over the subglacial channel connecting to the central channel, there is a sudden ten-fold increase in the rate of surface thinning beginning around 2015 (CCh) and a three-fold increase as far as ∼7 km upstream of the grounding line (CUp) by the following year. It appears this onset of thinning may be unique to the central channel, as there is no similar pattern upstream of the grounding line along the northern subglacial drainage route (NCh; there is insufficient data to construct an elevation time series along the southern drainage route), nor is there any detectable change in the rate of thinning at a typical "background" point (BG).

3.2 Dynamics of N79

The NW-SE lateral dichotomy may be due to rheological heterogeneity in the ice tongue. N79 contains both ice from NEGIS, which originates in a region of elevated geothermal heat (Rogozhina et al., 2016), and from a tributary that merges from the west very near the outlet, which is likely to be colder and less plastic. Thus, stress may be more prone to build up in SEIS, being accommodated more sporadically and explosively than in NWIS. The inferred surface strain rates (Figs. 4, S7) seem to confirm this. Entering the confines of the fjord imposes along-flow compressive strain on the ice tongue. In NWIS, the compression is fairly uniform, but in SEIS it is specifically concentrated along the flow-perpendicular channels, perhaps explaining their complex morphology and narrowing over time. More worrisome is the fact that shear strain has recently manifested along the central channel, suggesting the NWIS and SEIS halves of the ice tongue may be de-

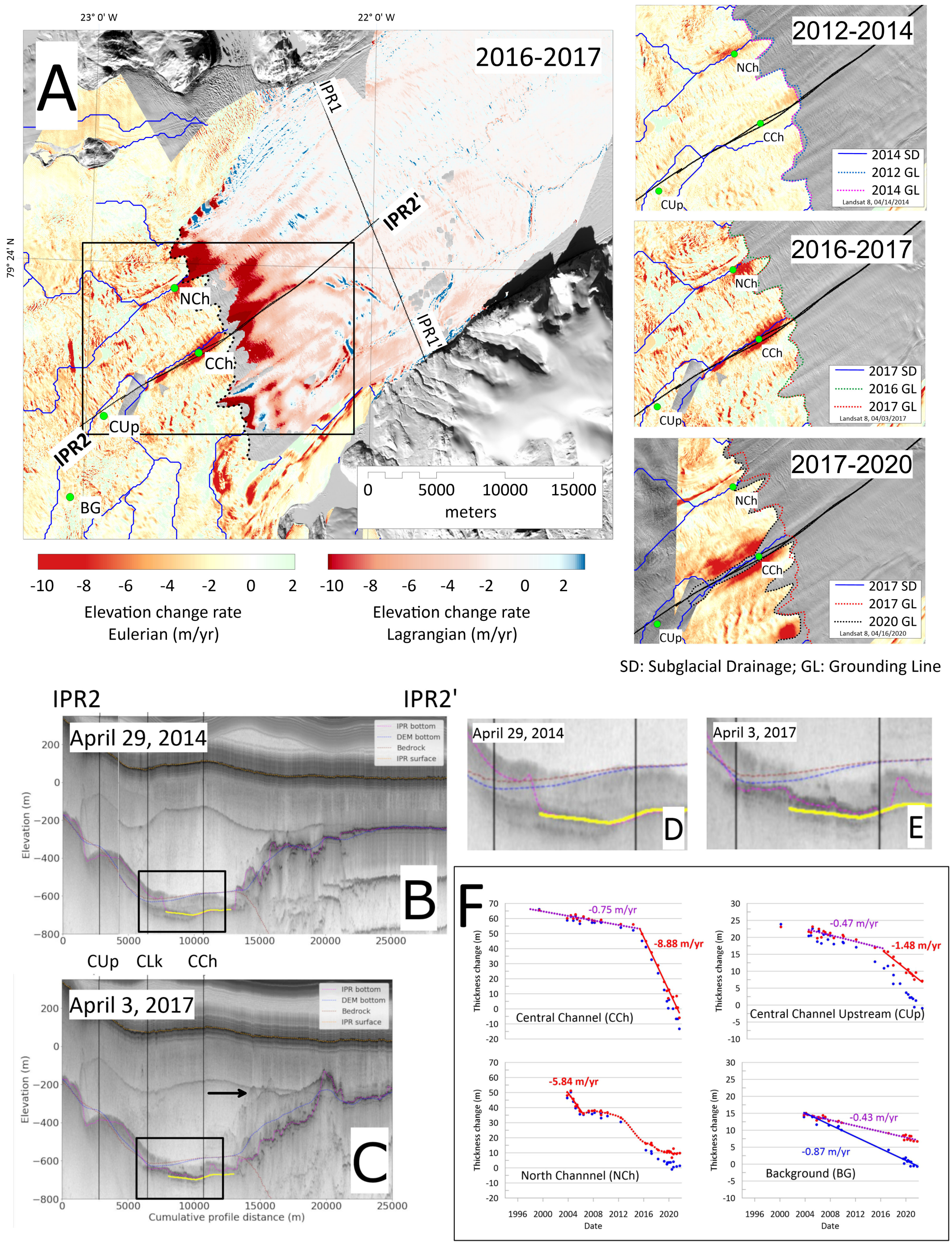

Figure 3. (A) Surface elevation change rate from 2016-17 showing the Eulerian difference on grounded ice and the Lagrangian difference on floating ice, with inferred major subglacial hydrologic pathways. Small maps on the right show the Eulerian annual elevation change rates near the grounding line for 2012-2014, 2016-2017, and 2017-2020. (B) Along-flow radar returns near the center line from 2014. (C) Radar returns from the same flight path on April 3, 2017. Note the thinning and increase in reflectivity (over the yellow line marking the 2014 ice bottom), and the side echo indicated by a black arrow. (D-G) Time series of elevation change for selected locations on grounded ice (green-filled circles in Fig. 3A). Total elevation change is shown in blue, and the dynamic component in red.

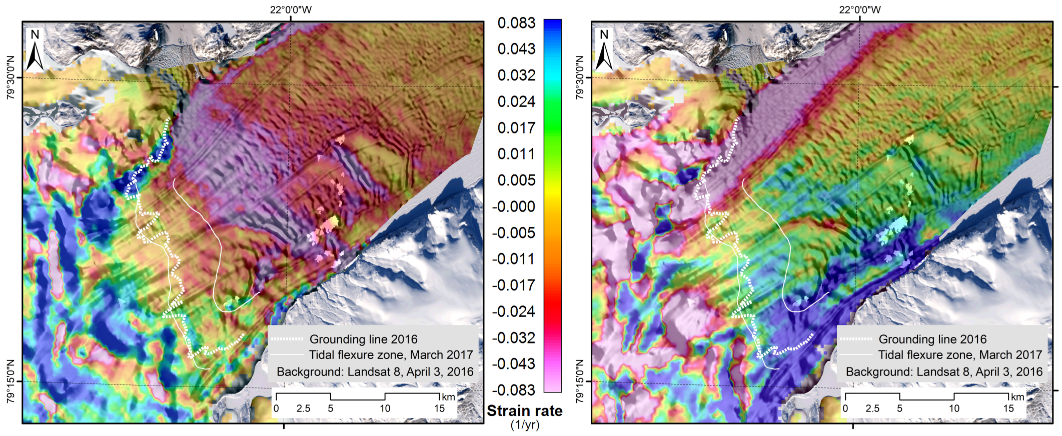

Figure 4. (A) Along-flow strain rate component inferred from the yearly average velocity 2016-17. (B) The corresponding shear strain rate component.

coupling as the channel becomes more incised. What effects this could have on the ice sheet's stability are not immediately obvious.

Yet, this regime of stress distribution and channel formation has existed since at least 1978 and does not appear to have caused thinning of this magnitude in the middle of the ice shelf until recently. The likely causes of this severe localized thinning are several-fold. It is probable that infiltration of warm AIW has increased, leading to more intense meltwater plume activity at the ice-ocean interface. Runoff rates have also continued to rise over the past few decades (Fig. S9), with 2012, when the most recent flow-perpendicular channel formed, being a year of particularly intense melting (Nghiem et al., 2012), with significant calving events across northern Greenland (Ochwat et al., 2022). Moreover, the non-perpendicular angle of the attached flow-perpendicular channel and the shift in basal drainage patterns could make the central channel a particularly conducive conduit for housing an active meltwater plume

4 Conclusion

Despite its complicated system of subglacial channels, we find that N79 was relatively stable for many years (at least from 1978-2012). A flow-perpendicular channel/central channel complex would appear and grow modestly for 5-10 years, but that growth would significantly diminish when a new flow-perpendicular channel appears and the old one begins to stagnate. One might liken this to the configuration of Jakobshavn Glacier prior to the disintegration of its floating icetongue in 1998 (Thomas et al., 2003). Like N79, Jakobshavn is sourced from two tributaries and had a large basal channel near the grounding line along the seam between these two branches. This channel began to grow, likely as a result of thickening of the warm water layer at the bottom of the fjord (Motyka et al., 2011). However, disintegration did not occur until the channel drew close to the calving front, and for the central channel of N79 this is decades away. There is also a resemblance to recent events at Petermann Glacier, which has a similarly long ice shelf, where grounding line retreat has been facilitated by rising ocean temperature (Washam et al., 2019) and fractures causing sections of the ice to become decoupled from one another (Millan et al., 2022).

While the impact of these developments on the ice sheet may not be felt for many years, there are still several insights to be gained. Firstly, the importance of continued high-density data collection must be stressed. Such observations cannot be made without a high spatiotemporal density of altimetry, DEMs, and surface velocities. Ideally, there would also be a greater density of radar observations, as there are presently no more effective methods of determining the true shape of the ice shelf bottom, and the available data was insufficient to meet the full needs of this research. Furthermore, the observed changes occur so quickly and are so localized that they would be very difficult to detect without processing such as that described here of combining datasets to improve their collective accuracy.

Perhaps more significantly, the results also hint at the weaknesses of our current fundamental ability to model ice sheets. The channels of N79 and their varied behavior are too small-scale and temporally variable to be easily incorporated in a model, yet the effects are rather dramatic. Simply turning up the ocean temperature beneath a generalized model of the N79 ice shelf is unlikely to result in the shelf being nearly split in two so close to the grounding line; and generalizing from localized data could be misleading. Consider Mayer et al. (2018), which reconstructs the mass loss of N79 largely based on observations of a single feature near the NWIS margin. We conclude that such an approach is misleading, given the non-uniformity in the pattern of thinning of N79. It is our hope that other researchers will continue to strive for greater density and accuracy of data, and increased model complexity. The tools developed for this research, once made publicly available, should assist in this regard, as they allow for more accurate elevation reconstruction of floating ice, and areas where adequate ice-free control surfaces are unavailable.

5 Open Research

The software used to generate the elevation reconstructions is the Mosaic Utility and Large Dataset Integration for SERAC (MOULINS) (Narkevic, 2021), which is still in development for public release. It includes spline-based curve fitting based on (Shekhar et al., 2021), and tidal correction based on software available at (`https://github.com/tsutterley/pyTMD`). The altimetry data used come from the Airborne Topographic Mapper (ATM; `https://nsidc.org/data/ilatm2/versions/2`), ICESat (`https://nsidc.org/data/glah12/versions/34`), and ICESat-2 (`https://nsidc.org/data/atl06/versions/4`). Uncorrected DEMs from 2012-2020, generated from WorldView imagery by the ArcticDEM project and are available at `https://data.pgc.umn.edu/elev/dem/setsm/ArcticDEM/strips/s2s041/2m`. The 1978 DEM is from `https://www.ncei.noaa.gov/access/metadata/landing-page/bin/iso?id=gov.noaa.nodc:0145405`. Surface elevations outside the reconstructed region are from BedMachine v4 (Morlighem et al., 2017), available at `https://nsidc.org/data/idbmg4/versions/4`, and the bed elevation is from (An et al., 2021), available `https://datadryad.org/stash/dataset/doi:10.7280/D19987`. Subglacial drainage reconstructions are made with Topo Toolbox (Schwanghart & Nikolaus, 2010), available at `https://topotoolbox.wordpress.com/`. The velocities used can be found at `https://datadryad.org/stash/dataset/doi:10.7280/D11H3X`. N79 calving fronts are from (Goliber et al., 2022) and available at from `https://doi.org/10.5281/zenodo.6557981`. All Landsat imagery is courtesy of USGS and obtained from `https://earthexplorer.usgs.gov/`. All new data sets generated by this study (surface elevation mosaics, corresponding ice bottom elevation, Lagrangian elevation change, and select partitioned time series), are accessible through Zenodo `https://doi.org/10.5281/zenodo.7518206`.

Acknowledgments

The authors wish to thank Laurie Padman and Susan L. Howard for assistance with tidal corrections, and Cornelis van der Veen for helpful discussion. This research was made possible with the following funding: NASA Sea-Level Change Team (Grant 80NSSC17K0611), ICESat-2 Science Team (Grant 80NSSC21K0915), and NSF Polar and Cyberinfrastructure programs (Grant OAC-2004826).

References

An, L., Rignot, E., Wood, M., Willis, J., Mouginot, J., & Khan, S. (2021). Ocean melting of the Zachariae Isstrøm and Nioghalvfjerdsfjorden glaciers, northeast Greenland. *Proceedings of the National Academy of Sciences*, *118*(2). doi: 10.1073/pnas.2015483118

Bentley, M., Smith, J., Jamieson, S., Lindeman, M., Rea, B., Humbert, A., ... Roberts, D. (2022). Direct measurement of warm Atlantic Intermediate Water close to the grounding line of Nioghalvfjerdsfjorden (79N) Glacier, North-east Greenland. *The Cryosphere Discussions*, *2022*, 1–25. doi: 10.5194/tc-2022-206

Brils, M., Kuipers Munneke, P., van de Berg, W. J., & van den Broeke, M. (2022). Improved representation of the contemporary Greenland ice sheet firn layer by IMAU-FDM v1.2G. *Geoscientific Model Development*, *15*(18), 7121–7138. doi: 10.5194/gmd-15-7121-2022

Choi, Y., Morlighem, M., Rignot, E., Mouginot, J., & Wood, M. (2017). Modeling the response of Nioghalvfjerdsfjorden and Zachariae Isstrøm glaciers, Greenland, to ocean forcing over the next century. *Geophysical Research Letters*, *44*(21), 11071-11079. doi: 10.1002/2017gl075174

CReSIS. (2020). *L1B Geolocated Radar Echo Strength Profile Images Data* [Dataset]. Digital Media. doi: data.cresis.ku.edu/data/rds/

Csatho, B., Schenk, A., van der Veen, C., Babonis, G., Duncan, K., Rezvanbehbahani, S., ... van Angelen, J. (2014). Laser altimetry reveals complex pattern of greenland ice sheet dynamics. *Proceedings of the National Academy of Sciences*, *111*(52), 18478-18483. doi: 10.1073/pnas.1411680112

ESA. (2017). *ESA Greenland Icesheet CCI, Grounding Lines from SAR Interferometry* [Dataset].

Goliber, S., Black, T., Catania, G., Lea, J. M., Olsen, H., Cheng, D., ... Zhang, E. (2022). TermPicks: a century of Greenland glacier terminus data for use in scientific and machine learning applications. *The Cryosphere*, *16*(8), 3215–3233. doi: 10.5194/tc-16-3215-2022

Howat, I., Negrete, A., & Smith, B. (2014). The Greenland Ice Mapping Project (GIMP) land classification and surface elevation data sets. *The Cryosphere*, *8*(4), 1509-1518. doi: 10.5194/tc-8-1509-2014

Khan, S., Choi, Y., Morlighem, M., Rignot, E., Helm, V., Humbert, A., ... Bjørk, A. (2022). Extensive inland thinning and speed-up of Northeast Greenland Ice Stream. *Nature*, *611*, 727-732. doi: 10.1038/s41586-022-05301-z

Korsgaard, N., Nuth, C., Khan, S., Kjeldsen, K., Bjørk, A., Schomacker, A., & Kjær, K. (2016). Digital elevation model and orthophotographs of Greenland based on aerial photographs from 1978–1987. *Scientific Data*, *3*(1), 160032. doi: 10.1038/sdata.2016.32

Larsen, N., Levy, L., Carlson, A., Buizert, C., Olsen, J., Strunk, A., ... Skov, D. (2018). Instability of the Northeast Greenland Ice Stream over the last 45,000 years. *Nature Communications*, *9*(1), 1-8. doi: 10.1038/s41467-018-04312-7

Mayer, C., Schaffer, J., Hattermann, T., Floricioiu, D., Krieger, L., Dodd, P., ... Schannwell, C. (2018). Large ice loss variability at Nioghalvfjerdsfjorden Glacier, Northeast-Greenland. *Nature Communications*, *9*(1), 1-11. doi: 10.1038/s41467-018-05180-x

Millan, R., Mouginot, J., Derkacheva, A., Rignot, E., Milillo, P., Ciraci, E., ... Bjørk, A. (2022). Ongoing grounding line retreat and fracturing initiated at the Petermann Glacier ice shelf, Greenland, after 2016. *The Cryosphere*, *16*(7), 3021–3031. doi: 10.5194/tc-16-3021-2022

Morlighem, M., Williams, C., Rignot, E., An, L., Arndt, J., Bamber, J., ... Zinglersen, K. (2017). BedMachine v3: Complete bed topography and ocean bathymetry mapping of Greenland from multibeam echo sounding combined with mass conservation. *Geophysical Research Letters*, *44*(21), 11,051-11,061.

doi: 10.1002/2017GL074954

Motyka, R., Truffer, M., Fahnestock, M., Mortensen, J., Rysgaard, S., & Howat, I. (2011). Submarine melting of the 1985 Jakobshavn Isbræ floating tongue and the triggering of the current retreat. *Journal of Geophysical Research: Earth Surface*, *116*(F1). doi: 10.1029/2009JF001632

Mouginot, J., Rignot, E., Bjørk, A., van den Broeke, M., Millan, R., Morlighem, M., ... Wood, M. (2019a). Forty-six years of greenland ice sheet mass balance from 1972 to 2018. *Proceedings of the National Academy of Sciences*, *116*(19), 9239-9244. doi: 10.1073/pnas.1904242116

Mouginot, J., Rignot, E., Scheuchl, B., Fenty, I., Khazendar, A., Morlighem, M., ... Paden, J. (2015). Fast retreat of Zachariæ Isstrøm, northeast Greenland. *Science*, *350*(6266), 1357-1361. doi: 10.1126/science.aac7111

Mouginot, J., Rignot, E., Scheuchl, B., Wood, M., & Millan, R. (2019b). *Annual ice velocity of the greenland ice sheet (2010-2017)* [Dataset]. UC Irvine. Retrieved from `https://datadryad.org/stash/dataset/doi:10.7280/D11H3X` doi: 10.7280/D11H3X

Narkevic, D. (2021). *Fusion of altimetry and Digital Elevation Models for change detection at the Northeast Greenland Ice Stream* (Doctoral dissertation, State University of New York at Buffalo). Retrieved from `https://www.proquest.com/openview/60e1c501f94c1bd5a0b3aa334ccce757/1?pq-origsite=gscholar&cbl=18750&diss=y`

Narkevic, D., Csatho, B., & Schenk, T. (2020). Rapid thinning at the grounding line of Northeast Greenland's N79 Glacier revealed by new elevation reconstruction. *Abstract C028-0017, Presented at the 2020 AGU Fall Meetings*.

Nghiem, S., Hall, D., Mote, T., Tedesco, M., Albert, M., Keegan, K., ... Neumann, G. (2012). The extreme melt across the Greenland ice sheet in 2012. *Geophysical Research Letters*, *39*(20). doi: 10.1029/2012GL053611

Noh, M.-J., & Howat, I. M. (2018). IceBridge ATM L2 Icessn Elevation, Slope, and Roughness, Version 2 [Greenland]. *Boulder, Colorado USA. NASA National Snow and Ice Data Center Distributed Active Archive Center.*. Retrieved from `https:https://doi.org/10.5067/E9E9QSRNLYTK` doi: 10.5067/E9E9QSRNLYTK

Ochwat, N., Scambos, T., Fahnestock, M., & Stammerjohn, S. (2022). Characteristics, recent evolution, and ongoing retreat of Hunt Fjord Ice Shelf, northern Greenland. *Journal of Glaciology*, 1-14. doi: 10.1017/jog.2022.44

Porter, C., Morin, P., Howat, I., Noh, M., Bates, B., Peterman, K., ... Bojesen, M. (2022). *ArcticDEM – Strips, Version 4.1* [Dataset]. Harvard Dataverse, V1. Retrieved from `https://data.pgc.umn.edu/elev/dem/setsm/ArcticDEM/geocell/v3.0/2m` doi: 10.7910/DVN/OHHUKH

Reeh, N., Mayer, C., Olesen, O., Christensen, E., & Thomsen, H. (2000). Tidal movement of Nioghalvfjerdsfjorden glacier, northeast Greenland: Observations and modelling. *Annals of Glaciology*, *31*, 111-117. doi: 10.3189/172756400781820408

Rogozhina, I., Petrunin, A., Vaughan, A., Steinberger, B., Johnson, J., Kaban, M., ... Koulakov, I. (2016). Melting at the base of the Greenland ice sheet explained by Iceland hotspot history. *Nature Geoscience*, *9*(5), 366-369. doi: 10.1038/ngeo2689

Schaffer, J., Kanzow, T., von Appen, W., von Albedyll, L., Arndt, J., & Roberts, D. (2020). Bathymetry constrains ocean heat supply to Greenland's largest glacier tongue. *Nature Geoscience*, *13*(3), 227-231. doi: 10.1038/s41561-019-0529-x

Schenk, T., & Csatho, B. (2012). A new methodology for detecting ice sheet surface elevation changes from laser altimetry data. *IEEE Transactions on Geoscience and Remote Sensing*, *50*(9), 3302-3316. doi: 10.1109/TGRS.2011.2182357

Schenk, T., Csatho, B., Veen, C. V. D., & McCormick, D. (2014, 00). Fusion of multi-sensor surface elevation data for improved characterization of rapidly changing outlet glaciers in Greenland. *Remote Sensing of Environment*, *149*, 239 – 251. doi: 10.1016/j.rse.2014.04.005

Schwanghart, W., & Nikolaus, J. (2010). TopoToolbox: A set of Matlab functions for topographic analysis. *Environmental Modelling & Software*, *25*(6), 770-781. doi: 10.1016/j.envsoft.2009.12.002

Sergienko, O. (2013). Basal channels on ice shelves. *Journal of Geophysical Research: Earth Surface*, *118*(3), 1342-1355. doi: 10.1002/jgrf.20105

Shean, D., Joughin, I., Dutrieux, P., Smith, B., & Berthier, E. (2019). Ice shelf basal melt rates from a high-resolution digital elevation model (DEM) record for Pine Island Glacier, Antarctica. *The Cryosphere*, *13*(10), 2633–2656. doi: doi.org/10.5194/tc-13-2633-2019

Shekhar, P., Csatho, B., Schenk, A., Roberts, C., & Patra, A. (2021). ALPS: A Unified Framework for Modeling Time Series of Land Ice Changes. *IEEE Transaction on Geoscience and Remote Sensing*, *59*(8), 6466–6481. doi: 10.1109/TGRS.2020.3027190

Thomas, R., Abdalati, W., Frederick, E., Krabill, W., Manizade, S., & Steffen, K. (2003). Investigation of surface melting and dynamic thinning on Jakobshavn Isbræ, Greenland. *Journal of Glaciology*, *49*(165), 231-239. doi: 10.3189/172756503781830764

van Wessem, J. M., van de Berg, W. J., Noël, B. P. Y., van Meijgaard, E., Amory, C., Birnbaum, G., … van den Broeke, M. R. (2018). Modelling the climate and surface mass balance of polar ice sheets using RACMO2 – Part 2: Antarctica (1979–2016). *The Cryosphere*, *12*(4), 1479–1498. doi: 10.5194/tc-12-1479-2018

Washam, P., Nicholls, K., Münchow, A., & Padman, L. (2019). Summer surface melt thins Petermann Gletscher Ice Shelf by enhancing channelized basal melt. *Journal of Glaciology*, *65*(252), 662–674. doi: 10.1017/jog.2019.43

Wilson, N., Straneo, F., & Heimbach, P. (2017, 00). Satellite-derived submarine melt rates and mass balance (2011–2015) for Greenland's largest remaining ice tongues. *The Cryosphere*, *11*(6), 2773 – 2782. doi: 10.5194/tc-11-2773-2017

Rapid basal channel growth beneath Greenland's longest floating ice shelf

Ash Narkevic[1], Bea Csatho[1], Toni Schenk[1]

[1]Department of Geological Sciences, University at Buffalo, Buffalo, NY, USA.

Corresponding author: A. Narkevic, davidnar@buffalo.edu

Abstract

Nioghalvfjerdsfjorden Glacier (N79) is one of the two main outlets for Greenland's largest ice stream, the Northeast Greenland Ice Stream (NEGIS), and is the more stable of the two, with no calving front retreat expected in the near future. Using a novel elevation reconstruction approach combining digital elevation models (DEMs) and laser altimetry, previously undetected local phenomena are identified complicating this assessment. N79 is found to have a complex network of basal channels that were largely stable between 1978 and 2012. Since then, an along-flow central basal channel has been growing rapidly, likely due to increased runoff and ocean temperatures, and possibly threatening to decouple the glacier's northwestern and southeastern halves.

1 Introduction

The Northeast Greenland Ice Stream (NEGIS) is the largest ice stream of the Greenland Ice Sheet, draining approximately 12% of its surface area and containing a sea-level rise equivalent of 1.1 m (Mouginot et al., 2015). Its discharge is routed through two major outlet glaciers, Zachariæ Isstrøm (ZI) and Nioghalvfjerdsfjorden Glacier (N79) (Fig. 1), the former of which has demonstrated a pattern of accelerating mass loss in recent decades (Mouginot et al., 2019a). N79 features a ∼70 km long floating ice tongue which provides a substantial buttressing effect to this branch of the ice stream (Mayer et al., 2018). At the end of its containing fjord, the ice tongue terminates upon a sill (Morlighem et al., 2017; An et al., 2021).

N79 experienced only minor changes in calving front and grounding line position between 1978 and 2020 (Fig. 1A, Supporting Information Fig. S1), possibly as a result of this configuration. Moreover, models such as the Ice Sheet Systems Model (ISSM) suggest that its grounding line and calving front are unlikely to change significantly over the next century (Choi et al., 2017). However, cosmogenic exposure and radiocarbon dating of surrounding rocks indicate that both N79 and ZI have retreated well inland from their current extents during the Holocene (Larsen et al., 2018), indicating that N79 may be more sensitive to climate change than previously thought. Indeed, velocity measurements show that, while not as dramatically as ZI, N79 has accelerated noticeably in the vicinity of its grounding line (∼ 10%) in recent decades (Mouginot et al., 2015). Moreover, the average water temperature is increasing, and the depth to the upper interface of warm Atlantic Intermediate Water (AIW) is decreasing in the open sea beyond the calving front (Schaffer et al., 2020); and many other glaciers in northern Greenland saw an onset of widespread calving events over the last decade (Ochwat et al., 2022). More recently, evidence of warm AIW has even been found in a marginal surface lake near the N79 grounding line (Bentley et al., 2022).

Laser altimetry time series indicate a dynamic thinning of less than 0.5 m annually between 1999 and 2009 on N79 (Csatho et al., 2014), with longer time series revealing an increased rate of thinning since 2012, with total thinning reaching over 50 m by 2020 close to the grounding line near the center of the glacier (Narkevic et al., 2020). However, this is only observed in a few locations because the sparse spatial coverage of airborne laser altimetry between 2009-2018 (Supporting Information Fig. S2) obscured whether the effect was a minor localized phenomenon or a more widespread trend that largely evaded the available altimetry flight lines. This question has significant implications, as reconstructions based on altimetry (e.g., Khan et al., 2022) make broad conclusions about N79 and other glaciers based on these sparse data.

This uncertainty can be mitigated by including digital elevation models (DEMs), which have a much denser spatial distribution of elevation data, albeit at the cost of poorer precision than altimetry. Using altimetry as control data for correcting any systematic error present in DEMs from multiple years within the time frame of interest can produce a reconstruction with high spatiotemporal resolution and accuracy. Here we present a novel elevation reconstruction of the N79 grounding region using such a technique.

2 Methods

Repeat coverage of WorldView (WV) stereo satellite imagery since 2011 enables the determination of ice sheet elevation changes with high spatial resolution and accuracy (Porter et al., 2022; Shean et al., 2019). We used ArcticDEM strips, generated from WV images using the Surface Extraction with TIN-based Search-space Minimization (SETSM) approach (Noh & Howat, 2018), to reconstruct elevation changes in the N79 region between 2012-2020. These DEMs, calculated using satellite ephemeris information only without applying ground control, still have vertical errors on the order of 4 m (Porter et al., 2022), which is unsuitable for precise change detection and investigating ice dynamic processes of outlet glaciers. We developed a correction algorithm, based on the approach of Schenk et al. (2014) to reduce this error. Altimetry time series, serving as control, were generated from Operation IceBridge Airborne Topographic Mapper (ATM) airborne (1993-2019), ICESat (2003-2009) and ICESat-2 (2018-present) satellite data using the Surface Elevation Reconstruction and Change Detection (SERAC) method (Schenk & Csatho, 2012). A spline-based approximation algorithm (Shekhar et al., 2021) infers the elevation at the date of the DEM acquisition for each time series, and a third-order polynomial correction surface is fitted to the resulting residuals for a given DEM. Once added to the DEM, the error is reduced, and separate DEMs can be mosaicked together with minimal edge discontinuity and a final uncertainty on the order of $\sim$1 m (Supporting Information Text S1). The pipeline also accounts for tidal flexure and the inverse barometric effect on floating ice (Supporting Information Text S2). In this manner, ice surface elevation DEMs, covering the N79 grounding line region, are created for 2012, 2014-2017, and 2020, with nominal dates in the spring to early summer (Supporting Information Table S1). The Greenland Ice Mapping Project (Howat et al., 2014) surface DEM is used outside the spatial extent of the corrected DEMs. A DEM generated from 1978 stereo aerial photographs (Korsgaard et al., 2016) is used for determining long-term elevation changes. Landsat and Sentinel imagery is used for qualitative assessment of surface features (e.g., Supporting Information Table S2).

The 2012-2020 gridded surface elevation reconstructions form the basis of several other data sets. Eulerian (static reference frame) annual elevation change is calculated as the direct difference between surface heights for consecutive years. Furthermore, using a hydrostatic assumption and a bathymetry model from An et al. (2021) as the bed elevation, the depth to the bottom of the ice shelf was inferred for each year and also used for estimating grounding line location (Supporting Information Text S3). The accuracy of the derived ice bottom elevations is assessed by comparing them with airborne ice-penetrating radar (IPR) returns (CReSIS, 2020). Basal drainage patterns are inferred for each year from the surface and bed DEMs using the MatLab Topo Toolbox (Schwanghart & Nikolaus, 2010), and tested for robustness using a Monte Carlo analysis as described in Narkevic (2021). Using this reconstructed basal routing to demarcate a basal drainage basin for N79, annual aggregate runoff is estimated using values from the Regional Atmospheric Climate Model v2.3p2 (van Wessem et al., 2018), assuming all runoff reaches the bed immediately.

Velocities for the period of interest, derived from a combination of radar and optical images using feature tracking and interferometry, are from Mouginot et al. (2019b). These are summer-to-spring annual averages from 2012-2017. From these, the surface strain rate components are derived and used as a proxy for surface stresses, and have an estimated uncertainty of $\sim$0.01 yr^{-1} based on the uncertainty in velocity. Eulerian change rates on floating ice are complicated by the advection of large fractures, so the velocities are used to reconstruct Lagrangian (moving reference frame) elevation changes for this region, i.e., taking the difference between elevation at an initial pixel, and the pixel to which that ice parcel would have advected by the subsequent DEM date (Supporting Information Text S4). This is performed in the manner of Shean et al. (2019).

Finally, to investigate the propagation of dynamic thinning to the grounded ice, SERAC time series derived from altimetry were partitioned into components due to surface processes as estimated by the IMAU-FDM v1.2G model (Brils et al., 2022) and ice dynamics.

3 Results

The cause of the anomalous rapid thinning detected by some SERAC time series is immediately apparent when comparing reconstructions from different years: a large along-flow channel appears in the center of the ice shelf near the grounding line, which experiences a higher rate of thinning than the surrounding ice (Fig. 1B and D-F). Moreover, it is not a novel feature of the ice, but part of an existing pattern of channels that has become increasingly exaggerated over time.

3.1 Morphology of N79

The floating ice shelf of N79 exhibits a lateral dichotomy. The northwestern ice shelf (NWIS) gradually becomes thinner with distance from the grounding line and is marked by a relatively uniform pattern of crevasses, while the southeastern ice shelf (SEIS) is characterized by larger, sparser flow-perpendicular channels separated by ∼5-10 km with surface bulges in between (Figs. 1B, 2A) The bulges create an across-flow step-wise thickness discontinuity up to ∼100 m at the center of the floating tongue (Reeh et al., 2000, Fig. 1C). This pattern remains visible within ∼40 km of the grounding line, beyond which the two halves appear more uniform. There are also three major along-flow channels, one at each margin, and one in the center. The central channel is less uniform than the others, consisting of segments trailing upstream from the northwest end of the SEIS flow-perpendicular channels. Around 2000, a second band of channels with a more oblique orientation appeared closer to the margin, essentially on top of the SEIS marginal channel (Fig. 1B yellow features), one of which causes the southern channel to fork (i.e., Figs. 1C, 1E). Overall, between 1978 and 2020, the ice sheet has become thinner, with more intense and complex channelization, with several channels reaching the grounding line by 2020 (Figs. 1D-F, Supporting Information Figs. S1B, S5).

The flow-perpendicular channels in SEIS are not necessarily analogous to the crevasses in NWIS. Near the grounding line, one can observe annual ”ripples” in the ice sheet that first appear angled upstream toward the center and are reminiscent of the basal channel pattern predicted for hetereogenous ice tongues under no-slip conditions by Sergienko (2013), and may represent the nascent form of the large flow-perpendicular channels. These generally rotate until perpendicular to flow, and some ultimately grow a new segment of the central channel, forming a hook shape, and developing a complex surface morphology with internal ridges (Fig. 2B). If in hydrostatic equilibrium, these ridges would correspond to subglacial keels, or they may be uncompensated compressional features. There are no radar flights spanning the flow-perpendicular channels to indicate which is the case. Over time (i.e., with distance from the grounding line), the flow-perpendicular channels tend to become narrower along-flow and more subdued in vertical relief.

Around 2012, two flow-perpendicular channels emerged near the grounding line in close proximity, the second of which did not fully rotate into flow-perpendicular position in subsequent years (Fig. 1B). The central channel segment connected to this flow-perpendicular channel has since grown, thinning the ice in its location at a prodigious rate, reaching nearly 100 myr^{-1} between 2017-2020 at the intersection of the transects in Figs. 2C-2D. This thinning is nearly twice the 50 myr^{-1} melt rate detected in 2011-2015 near the grounding line (Wilson et al., 2017). SERAC time series indicate the ef-

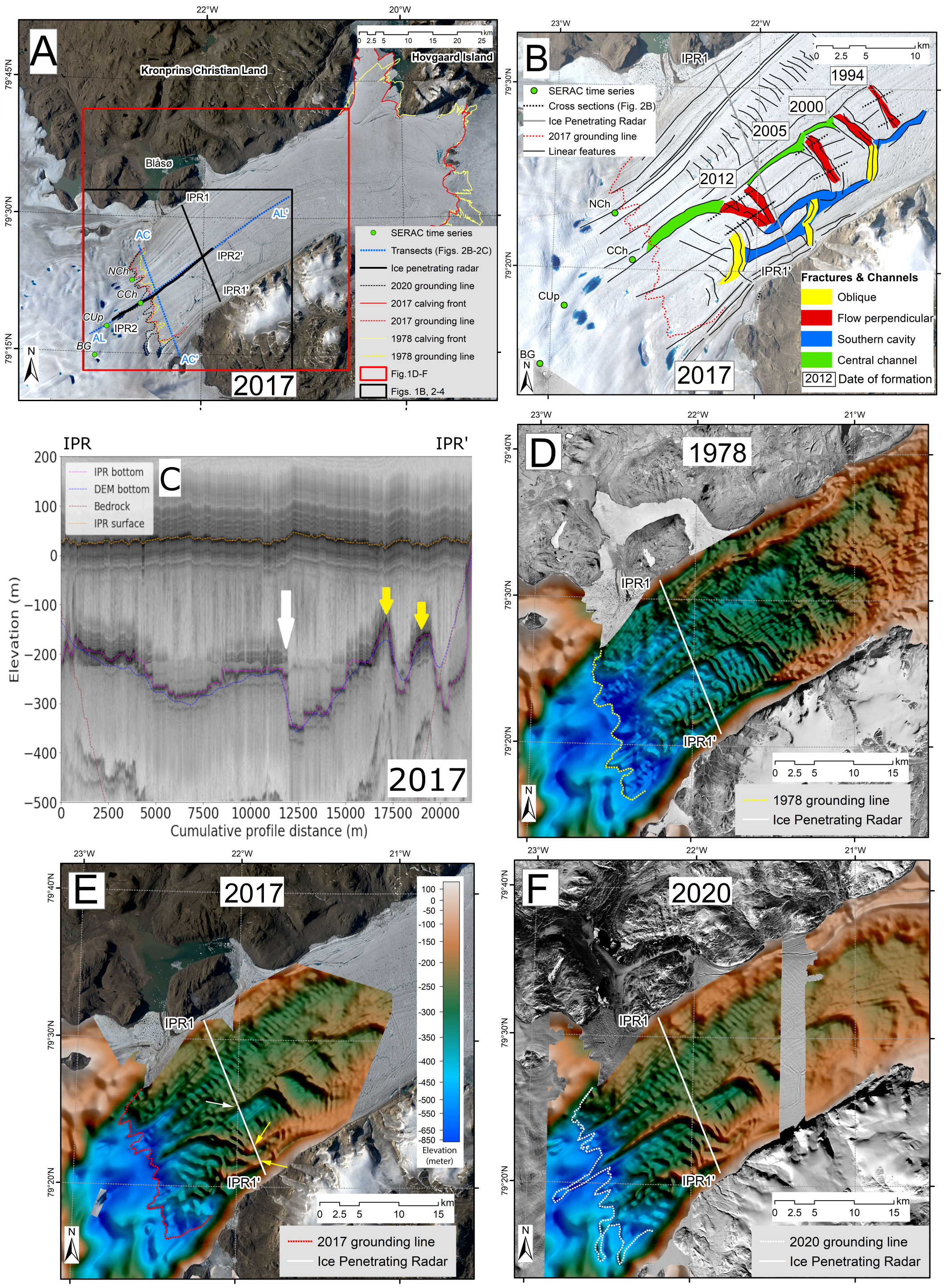

Figure 1. (A) Map of the study area showing calving-front and grounding-line changes between 1978 and 2020, and the locations of transects and SERAC times series. The larger box marks the area shown in Figs. 1D-1E, and the smaller box in Figs. 1B, 2-4, and Supporting Information Figs. S5-7. (B) Interpretation of observable surface features, with the year of formation for flow-perpendicular channels. (C) IPR profile from April 3, 2017, showing the abrupt flow-perpendicular thickness change across the center (white arrow) and the (forked) southeast marginal channel (yellow arrows, see arrows also in Fig. 1E). (D) 1978 ice bottom reconstruction, showing the buoyancy-inferred bottom depth for floating ice, and bedrock depth elsewhere. (E, F) Similar reconstructions for 2017 and 2020. Satellite images and aerial photographs shown in the figures are listed in Supporting Information Table S2.

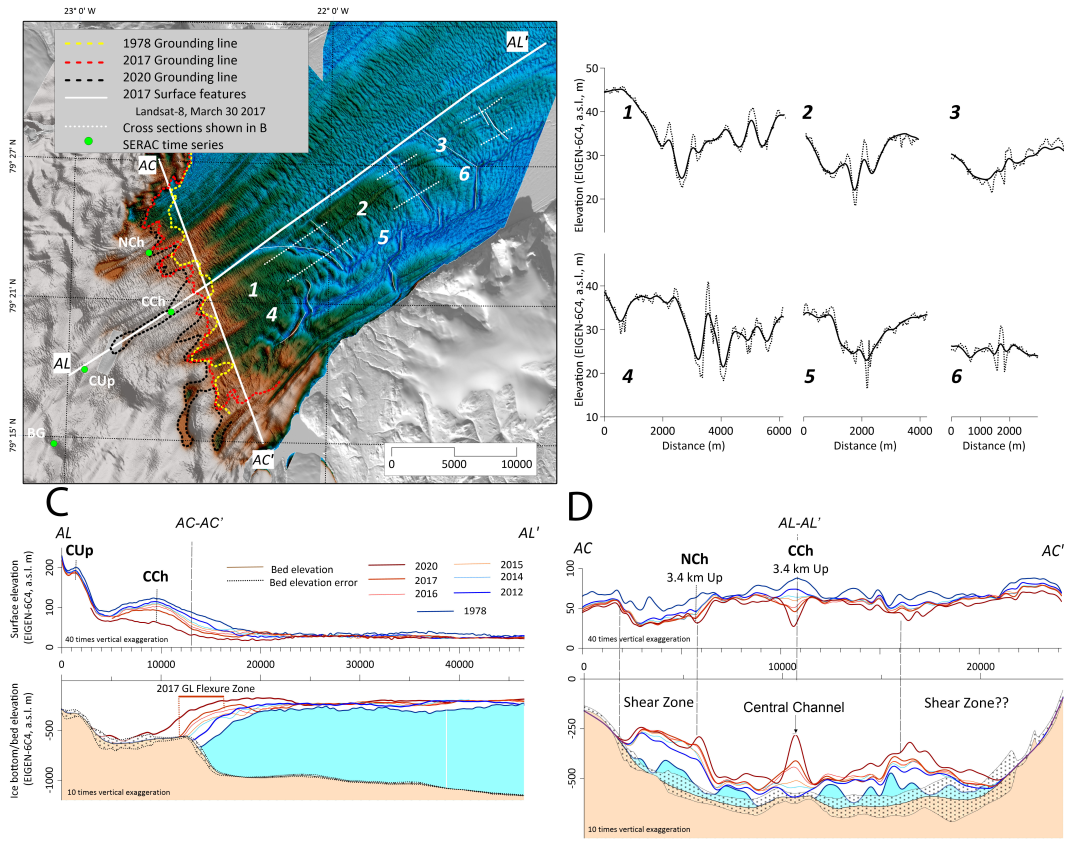

Figure 2. (A) Shaded relief ice surface elevation in 2017 with grounding line locations, ice shelf fractures from Landsat imagery, and locations of transects shown B. (B) Surface elevation profiles across flow-perpendicular channels, illustrating their complex morphology. Dotted lines show elevations from the 30-meter resolution DEM and solid lines from the DEM smoothed by a Gaussian kernel of 600 meter to emphasize surface topography reflecting basal channels. (C) Along and (D) Across-flow profiles of ice surface and bottom elevation showing central channel growth (C, D), grounding line retreat (C), and thinning in the shear zones (D). Shear zone extent is defined based on across-flow strain rates (Fig. 4B) and 2017 grounding line flexure zone is from (ESA, 2017)

fects were already detectable upstream of the grounding line by ∼2015 (Fig. 3F). Thinning continued along the basal channel and the connected subglacial channel (Figs. 3F, S6), and by 2020 the hydrostatically-inferred grounding line had experienced significant local retreat upstream of the central and SEIS marginal channels (Figs. 2A, 2C). This effect was sufficiently pronounced to shift the basal drainage patterns in the area. The potential basal drainage pathways from the reconstruction indicate three major outlets into the fjord: two corresponding to the marginal channels and one that, before 2016, entered the fjord about 1 km southeast of the central channel. By 2016 the channelized thinning shifted this pathway directly into the central channel (Fig. 3A, Supporting Information Fig. S5). The ensuing inferred grounding line retreat then proceeded along the central and southern basal drainage paths. These results, however, come with the caveat that the bed elevation in this area is uncertain and cannot be strongly claimed without additional evidence described below.

While there are no radar flights over the basal channel-subglacial channel system, inferences supporting its rapid thinning and corresponding grounding line retreat can be made from the 2014 and 2017 along-flow IPR transects, which are slightly southeast of and parallel to the channel (Fig. 3B-C). In the grounding zone (7500 to 13000 m along-track) one can see that the ice bottom horizon by 2017 has become both more reflective, indicating there is more water, and slightly higher. This suggests the area was grounded in 2014, and not fully grounded three years later. The ice bottom derived from surface elevation assuming hydrostatic equilibrium underestimates the bottom of the floating ice (Fig. 3C), suggesting that the ice is not in hydrostatic equilibrium. The 2017 radar profile also depicts the rapidly thinning ice shelf basal channel as a new "ghost" horizon ∼200 m above the ice bottom picks, which is likely a side echo from the bottom of the basal channel, about 100 m higher than it was in 2014 (Fig. 3B, 3C). One can also see the expression of the basal channel at the point where the flight crosses the hook-shaped connection between the central and 2012 flow-perpendicular channels, and it is even thinner than in the surface DEM-based reconstruction. Finally, the flattening of the ice sheet surface "bump" along the basal channel by 2020 (Fig. 2C, around CCh) also suggests the transition from grounded ice to floating ice conditions.

The increasing dynamic thinning of the grounded ice is illustrated by the SERAC elevation time series reconstructions shown in Fig. 3F. About 2.5 km upstream of the 2015-2017 grounding line over the subglacial channel connecting to the central channel, there is a sudden ten-fold increase in the rate of surface thinning beginning around 2015 (CCh) and a three-fold increase as far as ∼7 km upstream of the grounding line (CUp) by the following year. It appears this onset of thinning may be unique to the central channel, as there is no similar pattern upstream of the grounding line along the northern subglacial drainage route (NCh; there is insufficient data to construct an elevation time series along the southern drainage route), nor is there any detectable change in the rate of thinning at a typical "background" point (BG).

3.2 Dynamics of N79

The NW-SE lateral dichotomy may be due to rheological heterogeneity in the ice tongue. N79 contains both ice from NEGIS, which originates in a region of elevated geothermal heat (Rogozhina et al., 2016), and from a tributary that merges from the west very near the outlet, which is likely to be colder and less plastic. Thus, stress may be more prone to build up in SEIS, being accommodated more sporadically and explosively than in NWIS. The inferred surface strain rates (Figs. 4, S7) seem to confirm this. Entering the confines of the fjord imposes along-flow compressive strain on the ice tongue. In NWIS, the compression is fairly uniform, but in SEIS it is specifically concentrated along the flow-perpendicular channels, perhaps explaining their complex morphology and narrowing over time. More worrisome is the fact that shear strain has recently manifested along the central channel, suggesting the NWIS and SEIS halves of the ice tongue may be de-

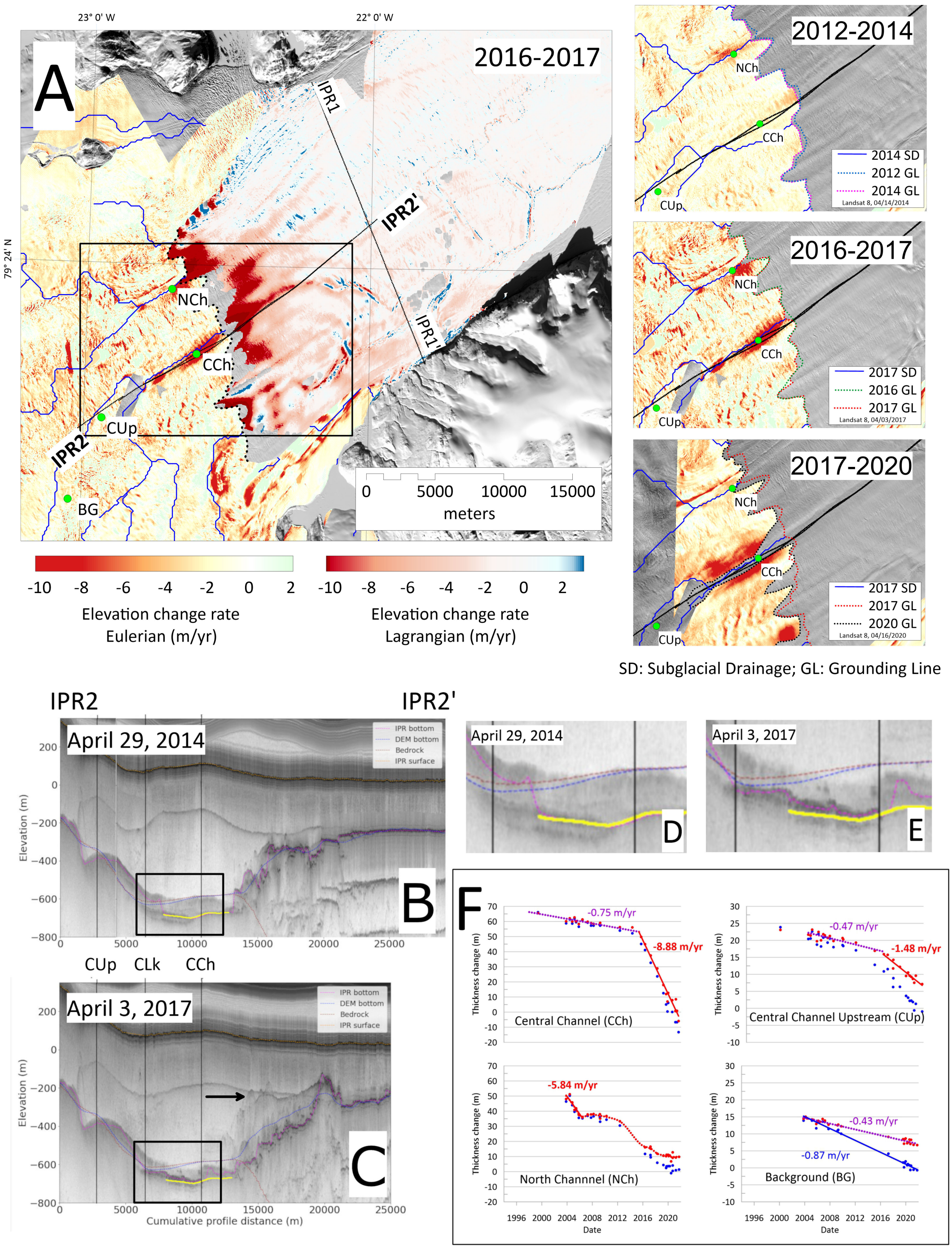

Figure 3. (A) Surface elevation change rate from 2016-17 showing the Eulerian difference on grounded ice and the Lagrangian difference on floating ice, with inferred major subglacial hydrologic pathways. Small maps on the right show the Eulerian annual elevation change rates near the grounding line for 2012-2014, 2016-2017, and 2017-2020. (B) Along-flow radar returns near the center line from 2014. (C) Radar returns from the same flight path on April 3, 2017. Note the thinning and increase in reflectivity (over the yellow line marking the 2014 ice bottom), and the side echo indicated by a black arrow. (D-G) Time series of elevation change for selected locations on grounded ice (green-filled circles in Fig. 3A). Total elevation change is shown in blue, and the dynamic component in red.

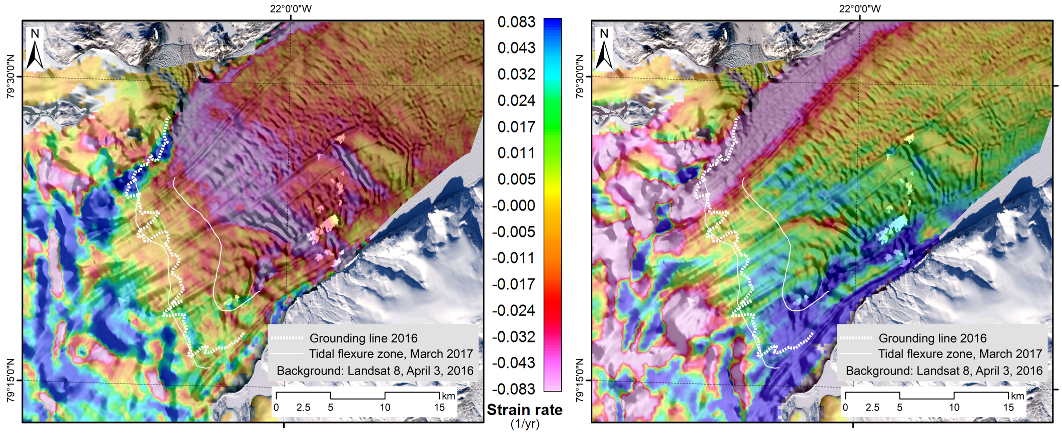

Figure 4. (A) Along-flow strain rate component inferred from the yearly average velocity 2016-17. (B) The corresponding shear strain rate component.

coupling as the channel becomes more incised. What effects this could have on the ice sheet's stability are not immediately obvious.

Yet, this regime of stress distribution and channel formation has existed since at least 1978 and does not appear to have caused thinning of this magnitude in the middle of the ice shelf until recently. The likely causes of this severe localized thinning are several-fold. It is probable that infiltration of warm AIW has increased, leading to more intense meltwater plume activity at the ice-ocean interface. Runoff rates have also continued to rise over the past few decades (Fig. S9), with 2012, when the most recent flow-perpendicular channel formed, being a year of particularly intense melting (Nghiem et al., 2012), with significant calving events across northern Greenland (Ochwat et al., 2022). Moreover, the non-perpendicular angle of the attached flow-perpendicular channel and the shift in basal drainage patterns could make the central channel a particularly conducive conduit for housing an active meltwater plume

4 Conclusion

Despite its complicated system of subglacial channels, we find that N79 was relatively stable for many years (at least from 1978-2012). A flow-perpendicular channel/central channel complex would appear and grow modestly for 5-10 years, but that growth would significantly diminish when a new flow-perpendicular channel appears and the old one begins to stagnate. One might liken this to the configuration of Jakobshavn Glacier prior to the disintegration of its floating icetongue in 1998 (Thomas et al., 2003). Like N79, Jakobshavn is sourced from two tributaries and had a large basal channel near the grounding line along the seam between these two branches. This channel began to grow, likely as a result of thickening of the warm water layer at the bottom of the fjord (Motyka et al., 2011). However, disintegration did not occur until the channel drew close to the calving front, and for the central channel of N79 this is decades away. There is also a resemblance to recent events at Petermann Glacier, which has a similarly long ice shelf, where grounding line retreat has been facilitated by rising ocean temperature (Washam et al., 2019) and fractures causing sections of the ice to become decoupled from one another (Millan et al., 2022).

While the impact of these developments on the ice sheet may not be felt for many years, there are still several insights to be gained. Firstly, the importance of continued high-density data collection must be stressed. Such observations cannot be made without a high spatiotemporal density of altimetry, DEMs, and surface velocities. Ideally, there would also be a greater density of radar observations, as there are presently no more effective methods of determining the true shape of the ice shelf bottom, and the available data was insufficient to meet the full needs of this research. Furthermore, the observed changes occur so quickly and are so localized that they would be very difficult to detect without processing such as that described here of combining datasets to improve their collective accuracy.

Perhaps more significantly, the results also hint at the weaknesses of our current fundamental ability to model ice sheets. The channels of N79 and their varied behavior are too small-scale and temporally variable to be easily incorporated in a model, yet the effects are rather dramatic. Simply turning up the ocean temperature beneath a generalized model of the N79 ice shelf is unlikely to result in the shelf being nearly split in two so close to the grounding line; and generalizing from localized data could be misleading. Consider Mayer et al. (2018), which reconstructs the mass loss of N79 largely based on observations of a single feature near the NWIS margin. We conclude that such an approach is misleading, given the non-uniformity in the pattern of thinning of N79. It is our hope that other researchers will continue to strive for greater density and accuracy of data, and increased model complexity. The tools developed for this research, once made publicly available, should assist in this regard, as they allow for more accurate elevation reconstruction of floating ice, and areas where adequate ice-free control surfaces are unavailable.

5 Open Research

The software used to generate the elevation reconstructions is the Mosaic Utility and Large Dataset Integration for SERAC (MOULINS) (Narkevic, 2021), which is still in development for public release. It includes spline-based curve fitting based on (Shekhar et al., 2021), and tidal correction based on software available at (`https://github.com/tsutterley/pyTMD`). The altimetry data used come from the Airborne Topographic Mapper (ATM; `https://nsidc.org/data/ilatm2/versions/2`), ICESat (`https://nsidc.org/data/glah12/versions/34`), and ICESat-2 (`https://nsidc.org/data/atl06/versions/4`). Uncorrected DEMs from 2012-2020, generated from WorldView imagery by the ArcticDEM project and are available at `https://data.pgc.umn.edu/elev/dem/setsm/ArcticDEM/strips/s2s041/2m`). The 1978 DEM is from `https://www.ncei.noaa.gov/access/metadata/landing-page/bin/iso?id=gov.noaa.nodc:0145405`. Surface elevations outside the reconstructed region are from BedMachine v4 (Morlighem et al., 2017), available at `https://nsidc.org/data/idbmg4/versions/4`, and the bed elevation is from (An et al., 2021), available `https://datadryad.org/stash/dataset/doi:10.7280/D19987`. Subglacial drainage reconstructions are made with Topo Toolbox (Schwanghart & Nikolaus, 2010), available at `https://topotoolbox.wordpress.com/`. The velocities used can be found at `https://datadryad.org/stash/dataset/doi:10.7280/D11H3X`. N79 calving fronts are from (Goliber et al., 2022) and available at from `https://doi.org/10.5281/zenodo.6557981`. All Landsat imagery is courtesy of USGS and obtained from `https://earthexplorer.usgs.gov/`. All new data sets generated by this study (surface elevation mosaics, corresponding ice bottom elevation, Lagrangian elevation change, and select partitioned time series), are accessible through Zenodo `https://doi.org/10.5281/zenodo.7518206`.

Acknowledgments
The authors wish to thank Laurie Padman and Susan L. Howard for assistance with tidal corrections, and Cornelis van der Veen for helpful discussion. This research was made possible with the following funding: NASA Sea-Level Change Team (Grant 80NSSC17K0611), ICESat-2 Science Team (Grant 80NSSC21K0915), and NSF Polar and Cyberinfrastructure programs (Grant OAC-2004826).

References

An, L., Rignot, E., Wood, M., Willis, J., Mouginot, J., & Khan, S. (2021). Ocean melting of the Zachariae Isstrøm and Nioghalvfjerdsfjorden glaciers, northeast Greenland. *Proceedings of the National Academy of Sciences*, *118*(2). doi: 10.1073/pnas.2015483118

Bentley, M., Smith, J., Jamieson, S., Lindeman, M., Rea, B., Humbert, A., ... Roberts, D. (2022). Direct measurement of warm Atlantic Intermediate Water close to the grounding line of Nioghalvfjerdsfjorden (79N) Glacier, North-east Greenland. *The Cryosphere Discussions*, *2022*, 1–25. doi: 10.5194/tc-2022-206

Brils, M., Kuipers Munneke, P., van de Berg, W. J., & van den Broeke, M. (2022). Improved representation of the contemporary Greenland ice sheet firn layer by IMAU-FDM v1.2G. *Geoscientific Model Development*, *15*(18), 7121–7138. doi: 10.5194/gmd-15-7121-2022

Choi, Y., Morlighem, M., Rignot, E., Mouginot, J., & Wood, M. (2017). Modeling the response of Nioghalvfjerdsfjorden and Zachariae Isstrøm glaciers, Greenland, to ocean forcing over the next century. *Geophysical Research Letters*, *44*(21), 11071-11079. doi: 10.1002/2017gl075174

CReSIS. (2020). *L1B Geolocated Radar Echo Strength Profile Images Data* [Dataset]. Digital Media. doi: data.cresis.ku.edu/data/rds/

Csatho, B., Schenk, A., van der Veen, C., Babonis, G., Duncan, K., Rezvanbehbahani, S., ... van Angelen, J. (2014). Laser altimetry reveals complex pattern of greenland ice sheet dynamics. *Proceedings of the National Academy of Sciences*, *111*(52), 18478-18483. doi: 10.1073/pnas.1411680112

ESA. (2017). *ESA Greenland Icesheet CCI, Grounding Lines from SAR Interferometry* [Dataset].

Goliber, S., Black, T., Catania, G., Lea, J. M., Olsen, H., Cheng, D., ... Zhang, E. (2022). TermPicks: a century of Greenland glacier terminus data for use in scientific and machine learning applications. *The Cryosphere*, *16*(8), 3215–3233. doi: 10.5194/tc-16-3215-2022

Howat, I., Negrete, A., & Smith, B. (2014). The Greenland Ice Mapping Project (GIMP) land classification and surface elevation data sets. *The Cryosphere*, *8*(4), 1509-1518. doi: 10.5194/tc-8-1509-2014

Khan, S., Choi, Y., Morlighem, M., Rignot, E., Helm, V., Humbert, A., ... Bjørk, A. (2022). Extensive inland thinning and speed-up of Northeast Greenland Ice Stream. *Nature*, *611*, 727-732. doi: 10.1038/s41586-022-05301-z

Korsgaard, N., Nuth, C., Khan, S., Kjeldsen, K., Bjørk, A., Schomacker, A., & Kjær, K. (2016). Digital elevation model and orthophotographs of Greenland based on aerial photographs from 1978–1987. *Scientific Data*, *3*(1), 160032. doi: 10.1038/sdata.2016.32

Larsen, N., Levy, L., Carlson, A., Buizert, C., Olsen, J., Strunk, A., ... Skov, D. (2018). Instability of the Northeast Greenland Ice Stream over the last 45,000 years. *Nature Communications*, *9*(1), 1-8. doi: 10.1038/s41467-018-04312-7

Mayer, C., Schaffer, J., Hattermann, T., Floricioiu, D., Krieger, L., Dodd, P., ... Schannwell, C. (2018). Large ice loss variability at Nioghalvfjerdsfjorden Glacier, Northeast-Greenland. *Nature Communications*, *9*(1), 1-11. doi: 10.1038/s41467-018-05180-x

Millan, R., Mouginot, J., Derkacheva, A., Rignot, E., Milillo, P., Ciraci, E., ... Bjørk, A. (2022). Ongoing grounding line retreat and fracturing initiated at the Petermann Glacier ice shelf, Greenland, after 2016. *The Cryosphere*, *16*(7), 3021–3031. doi: 10.5194/tc-16-3021-2022

Morlighem, M., Williams, C., Rignot, E., An, L., Arndt, J., Bamber, J., ... Zinglersen, K. (2017). BedMachine v3: Complete bed topography and ocean bathymetry mapping of Greenland from multibeam echo sounding combined with mass conservation. *Geophysical Research Letters*, *44*(21), 11,051-11,061.

doi: 10.1002/2017GL074954

Motyka, R., Truffer, M., Fahnestock, M., Mortensen, J., Rysgaard, S., & Howat, I. (2011). Submarine melting of the 1985 Jakobshavn Isbræ floating tongue and the triggering of the current retreat. *Journal of Geophysical Research: Earth Surface*, *116*(F1). doi: 10.1029/2009JF001632

Mouginot, J., Rignot, E., Bjørk, A., van den Broeke, M., Millan, R., Morlighem, M., ... Wood, M. (2019a). Forty-six years of greenland ice sheet mass balance from 1972 to 2018. *Proceedings of the National Academy of Sciences*, *116*(19), 9239-9244. doi: 10.1073/pnas.1904242116

Mouginot, J., Rignot, E., Scheuchl, B., Fenty, I., Khazendar, A., Morlighem, M., ... Paden, J. (2015). Fast retreat of Zachariæ Isstrøm, northeast Greenland. *Science*, *350*(6266), 1357-1361. doi: 10.1126/science.aac7111

Mouginot, J., Rignot, E., Scheuchl, B., Wood, M., & Millan, R. (2019b). *Annual ice velocity of the greenland ice sheet (2010-2017)* [Dataset]. UC Irvine. Retrieved from `https://datadryad.org/stash/dataset/doi:10.7280/D11H3X` doi: 10.7280/D11H3X

Narkevic, D. (2021). *Fusion of altimetry and Digital Elevation Models for change detection at the Northeast Greenland Ice Stream* (Doctoral dissertation, State University of New York at Buffalo). Retrieved from `https://www.proquest.com/openview/60e1c501f94c1bd5a0b3aa334ccce757/1?pq-origsite=gscholar&cbl=18750&diss=y`

Narkevic, D., Csatho, B., & Schenk, T. (2020). Rapid thinning at the grounding line of Northeast Greenland's N79 Glacier revealed by new elevation reconstruction. *Abstract C028-0017, Presented at the 2020 AGU Fall Meetings*.

Nghiem, S., Hall, D., Mote, T., Tedesco, M., Albert, M., Keegan, K., ... Neumann, G. (2012). The extreme melt across the Greenland ice sheet in 2012. *Geophysical Research Letters*, *39*(20). doi: 10.1029/2012GL053611

Noh, M.-J., & Howat, I. M. (2018). IceBridge ATM L2 Icessn Elevation, Slope, and Roughness, Version 2 [Greenland]. *Boulder, Colorado USA. NASA National Snow and Ice Data Center Distributed Active Archive Center.*. Retrieved from `https:https://doi.org/10.5067/E9E9QSRNLYTK` doi: 10.5067/E9E9QSRNLYTK

Ochwat, N., Scambos, T., Fahnestock, M., & Stammerjohn, S. (2022). Characteristics, recent evolution, and ongoing retreat of Hunt Fjord Ice Shelf, northern Greenland. *Journal of Glaciology*, 1-14. doi: 10.1017/jog.2022.44

Porter, C., Morin, P., Howat, I., Noh, M., Bates, B., Peterman, K., ... Bojesen, M. (2022). *ArcticDEM – Strips, Version 4.1* [Dataset]. Harvard Dataverse, V1. Retrieved from `https://data.pgc.umn.edu/elev/dem/setsm/ArcticDEM/geocell/v3.0/2m` doi: 10.7910/DVN/OHHUKH

Reeh, N., Mayer, C., Olesen, O., Christensen, E., & Thomsen, H. (2000). Tidal movement of Nioghalvfjerdsfjorden glacier, northeast Greenland: Observations and modelling. *Annals of Glaciology*, *31*, 111-117. doi: 10.3189/172756400781820408

Rogozhina, I., Petrunin, A., Vaughan, A., Steinberger, B., Johnson, J., Kaban, M., ... Koulakov, I. (2016). Melting at the base of the Greenland ice sheet explained by Iceland hotspot history. *Nature Geoscience*, *9*(5), 366-369. doi: 10.1038/ngeo2689

Schaffer, J., Kanzow, T., von Appen, W., von Albedyll, L., Arndt, J., & Roberts, D. (2020). Bathymetry constrains ocean heat supply to Greenland's largest glacier tongue. *Nature Geoscience*, *13*(3), 227-231. doi: 10.1038/s41561-019-0529-x

Schenk, T., & Csatho, B. (2012). A new methodology for detecting ice sheet surface elevation changes from laser altimetry data. *IEEE Transactions on Geoscience and Remote Sensing*, *50*(9), 3302-3316. doi: 10.1109/TGRS.2011.2182357

Schenk, T., Csatho, B., Veen, C. V. D., & McCormick, D. (2014, 00). Fusion of multi-sensor surface elevation data for improved characterization of rapidly changing outlet glaciers in Greenland. *Remote Sensing of Environment*, *149*, 239 – 251. doi: 10.1016/j.rse.2014.04.005

Schwanghart, W., & Nikolaus, J. (2010). TopoToolbox: A set of Matlab functions for topographic analysis. *Environmental Modelling & Software*, *25*(6), 770-781. doi: 10.1016/j.envsoft.2009.12.002

Sergienko, O. (2013). Basal channels on ice shelves. *Journal of Geophysical Research: Earth Surface*, *118*(3), 1342-1355. doi: 10.1002/jgrf.20105

Shean, D., Joughin, I., Dutrieux, P., Smith, B., & Berthier, E. (2019). Ice shelf basal melt rates from a high-resolution digital elevation model (DEM) record for Pine Island Glacier, Antarctica. *The Cryosphere*, *13*(10), 2633–2656. doi: doi.org/10.5194/tc-13-2633-2019

Shekhar, P., Csatho, B., Schenk, A., Roberts, C., & Patra, A. (2021). ALPS: A Unified Framework for Modeling Time Series of Land Ice Changes. *IEEE Transaction on Geoscience and Remote Sensing*, *59*(8), 6466–6481. doi: 10.1109/TGRS.2020.3027190

Thomas, R., Abdalati, W., Frederick, E., Krabill, W., Manizade, S., & Steffen, K. (2003). Investigation of surface melting and dynamic thinning on Jakobshavn Isbræ, Greenland. *Journal of Glaciology*, *49*(165), 231-239. doi: 10.3189/172756503781830764

van Wessem, J. M., van de Berg, W. J., Noël, B. P. Y., van Meijgaard, E., Amory, C., Birnbaum, G., … van den Broeke, M. R. (2018). Modelling the climate and surface mass balance of polar ice sheets using RACMO2 – Part 2: Antarctica (1979–2016). *The Cryosphere*, *12*(4), 1479–1498. doi: 10.5194/tc-12-1479-2018

Washam, P., Nicholls, K., Münchow, A., & Padman, L. (2019). Summer surface melt thins Petermann Gletscher Ice Shelf by enhancing channelized basal melt. *Journal of Glaciology*, *65*(252), 662–674. doi: 10.1017/jog.2019.43

Wilson, N., Straneo, F., & Heimbach, P. (2017, 00). Satellite-derived submarine melt rates and mass balance (2011–2015) for Greenland's largest remaining ice tongues. *The Cryosphere*, *11*(6), 2773 – 2782. doi: 10.5194/tc-11-2773-2017

Geophysical Research Letters

Supporting Information for

Rapid basal channel growth beneath Greenland's longest floating ice shelf

Ash Narkevic[1], Bea Csatho[1], Toni Schenk[1]

[1]Department of Geological Sciences, University at Buffalo, Buffalo, NY, USA

Contents of this file

Text S1 to S5
Figures S1 to S9
Tables S1 to S2

Introduction

This supplement contains supporting text, figures, and tables for "Rapid basal channel growth beneath Greenland's longest floating ice shelf."

Text S1. Ice sheet and ice shelf elevation from 1978-2020

The AERODEM tiles in the N79 region are derived from aerial photographs collected in July 1978. The AERODEM has a horizontal resolution of 25 m, a horizontal error of 10 m and a vertical error of 6 m, with vertical errors increasing from the coastal regions toward the interior (Korsgaard et l., 2016).

The WV DEMs have an original resolution of 2 m, and errors (both vertical and horizontal) are estimated to be around 4 m (Porter et al., 2022).

All DEMs are referenced to the WGS-84 ellipsoid and provided in UTM N-27 projection. Prior to correcting them we resampled the WV DEMs to 30 m resolution.

The uncertainty of a corrected WV DEM (δh_{DEM}) is derived derived from the respective uncertainties of the correction surface fitting (δh_c^2), and the time series curve fitting (δh_t^2), both of which as taken as the standard deviation of residuals according to:

$$\delta h_{DEM} = \sqrt{\delta h_c^2 - \delta h_t^2}$$

and is typically on the order of ~1m, which is a significant improvement over the original ~4m error.

Text S2 Corrections of floating ice elevations

The tide correction portion of the software used for these reconstructions is adapted from that used by Sutterly et al. (2019) using the tidal model of Padman et al. (2018). A tidal correction is applied to ice elevations at all points that are not grounded, however, it is assumed the effect is dampened near the grounding line and the sides of the outlet glacier. From InSAR measurement a tidal flexure zone extending 6 km downstream beyond the grounding line was detected in March 5, 2017 (ESA, 2017), and GPS measurements suggested a few km wide flexure zones inward from the fjord walls (Reeh et al., 2000). We used conservative estimates of 10 km and 2 km for the flexure zone width along the grounding line and the fjord walls, respectively. Within these zones, the tidal correction is scaled in a linear fashion from 100% of the modeled correction to 0% at the grounding line/fjord walls.

A correction is also applied to offset the inverse barometric effect:

$$\Delta IBE = \frac{p_{avg} - p_{loc}}{\rho_w g}$$

where p_{avg} is the global average atmospheric pressure, p_{loc} is the local atmospheric pressure, ρ_w is the density of seawater, and g is gravitational acceleration. Currently, this correction is only applied to ICESat and ICESat-2 data, as ATM data products do not include corresponding modeled atmospheric pressure information. For the example time series in Fig. S3 these corrections improved the standard deviation of the polynomial fit residual from 0.445 m to 0.216 m, and the standard deviation of the penalized spline fit residual (ALPS; Shekhar et al., 2021) from 0.336 m to 0.135 m.

Text S3. Ice Bottom Reconstruction

Additionally, the bathymetry used to infer grounding lines from the ice bottom reconstruction is taken from An et al. (2020). An assumption of hydrostatic equilibrium is made to reconstruct the elevation of the ice bottom from the ice surface DEMs. First, the DEMs are converted from the WGS-84 ellipsoid used by ArcticDEM strips and the ice sheet altimetry to the EIGEN-6C4 geoid (Foerste et al., 2014) to obtain the ice elevation above sea level. Densities of 1026 kg/m^3 for sea water and 917 kg/m^3 for glacier ice are assumed, thus making the estimated depth

8.4128 times greater than the surface elevation. If the calculated ice bottom elevation is below the bedrock elevation at a given location, the glacier is assumed to be grounded at that location, and the bed elevation is used as the ice bottom elevation.

Reconstructing the ice bottom in this manner creates a bottom surface that is extremely rugged, as the surface DEM captures many small-scale features which are likely to be out of precise equilibrium. Therefore, a gaussian filter with a kernel size of 21 pixels (equivalent to 600 meter) is applied to the ice bottom reconstructions presented in this paper.

The uncertainty of this data set is estimated by direct comparison with the radar measurements. The difference between the radar pick and calculated ice bottom after smoothing is calculated along a segment of the ice bottom that is relatively flat (18000 m – 25000 m in the 4/29/2014 radar profile in Fig. S4). The standard deviation of these differences is found to be 9.4m, and this is taken as representative of regions of the ice where the assumption of hydrostatic equilibrium is valid. Additionally, the mean difference was found to be 0.91m, suggesting minimal bias in this sample.

Text S4. Calculation of elevation change in a Lagrangian (moving) reference frame

In the final Lagrangian elevation change data product, the listed value is positioned at the end of the movement of the ice parcel. I.e., for a given starting pixel, the corresponding ending pixel is estimated using the velocity, and the difference between these two elevations is reported as the Lagrangian elevation change at the ending pixel (Fig. S6, floating ice).

The DEM reconstruction dates (Table S1) are generally representative of spring, and the annual velocity products used are the average from July 1st of one year to June 30th of the following year.

Text S5. Runoff Evolution

To quantify the change in runoff within the N79 drainage basin over time, it was first necessary to demarcate the extent of that basin. TopoToolbox lacked this functionality, so for these purposes the drainage reconstruction was performed in ArcMap. Since full DEMs exist only for a limited number of years, it is assumed that the subglacial drainage basin extent is static, and the 2017 DEM and bed DEM were used to calculate it. For each year from 1978 to 2016, all pixels within these bounds were identified in the RACMO v2.3p2 runoff dataset and summed. The results are illustrated in Fig. S8.

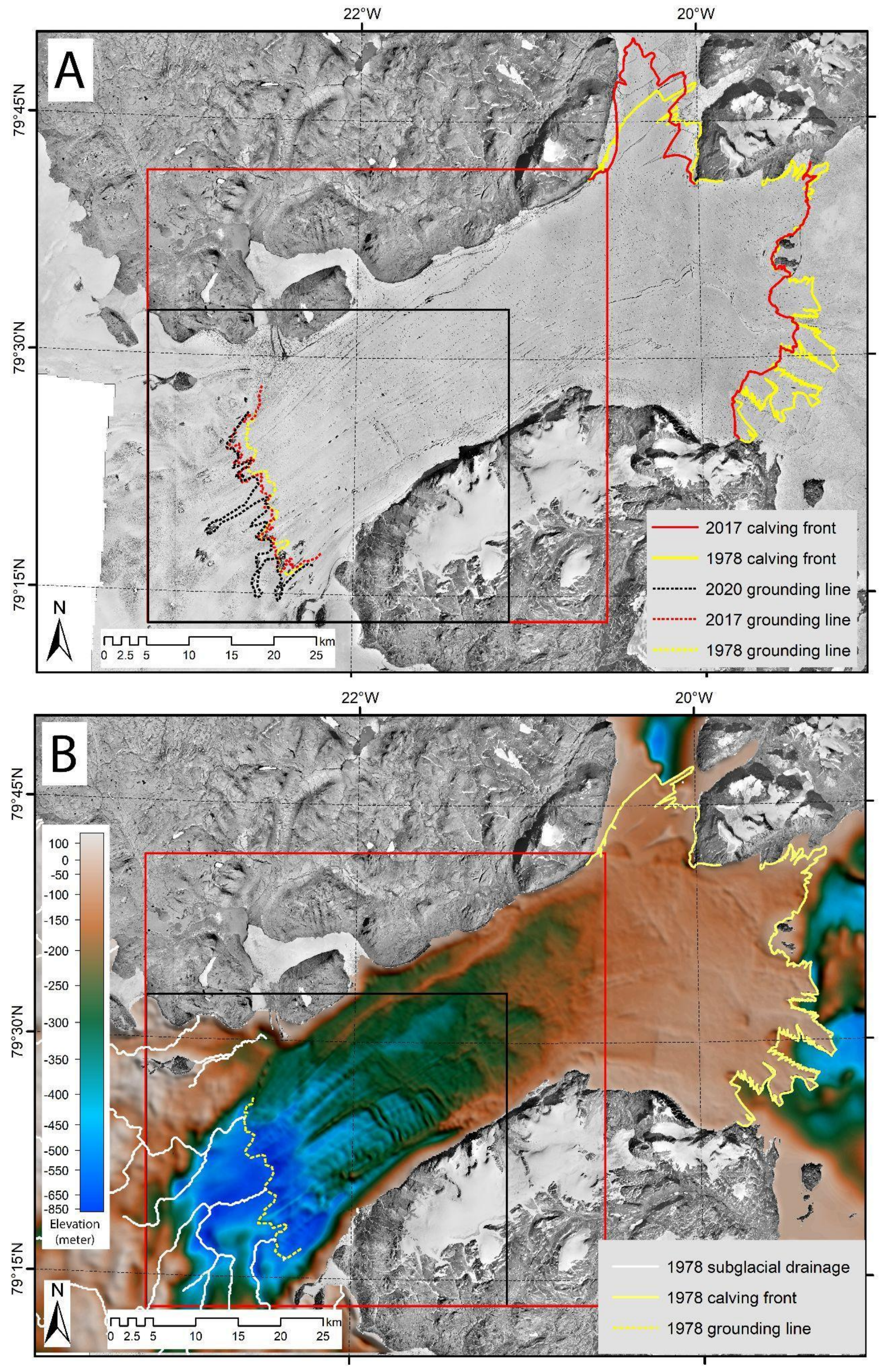

Figure S1. Surface features and ice bottom topography of N79 in 1978. (A) Aerial photo orthomosaic, (B) elevation of the ice bottom under the floating tongue, combined with bedrock elevation under the grounded ice sheet and the ocean.

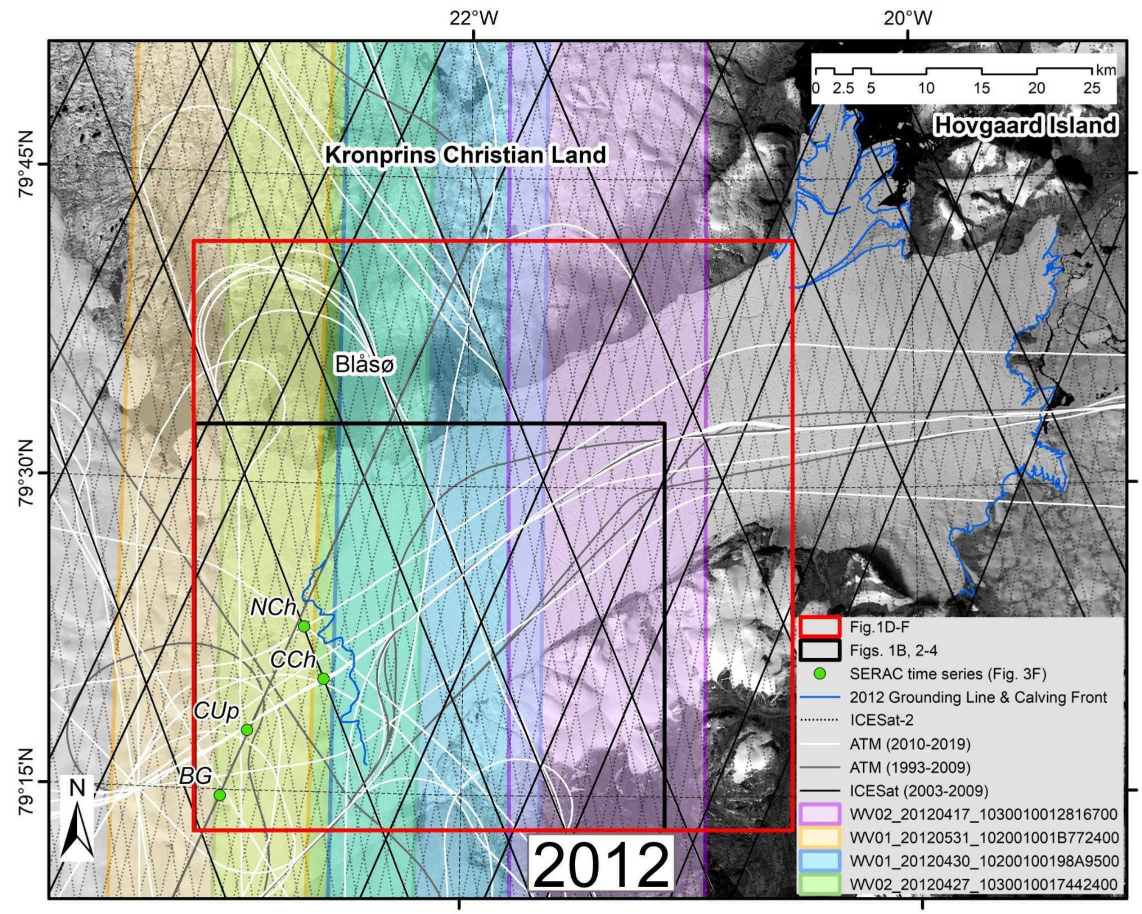

Figure S2. Location of four 2012 WorldView DEMs from a total of 14 used for generating the 2012 ice sheet elevation reconstruction (see Table S1 for complete list) with altimetry data locations (ATM, ICESat, ICESat-2) overlain. Background is a Landsat-8 imagery mosaic.

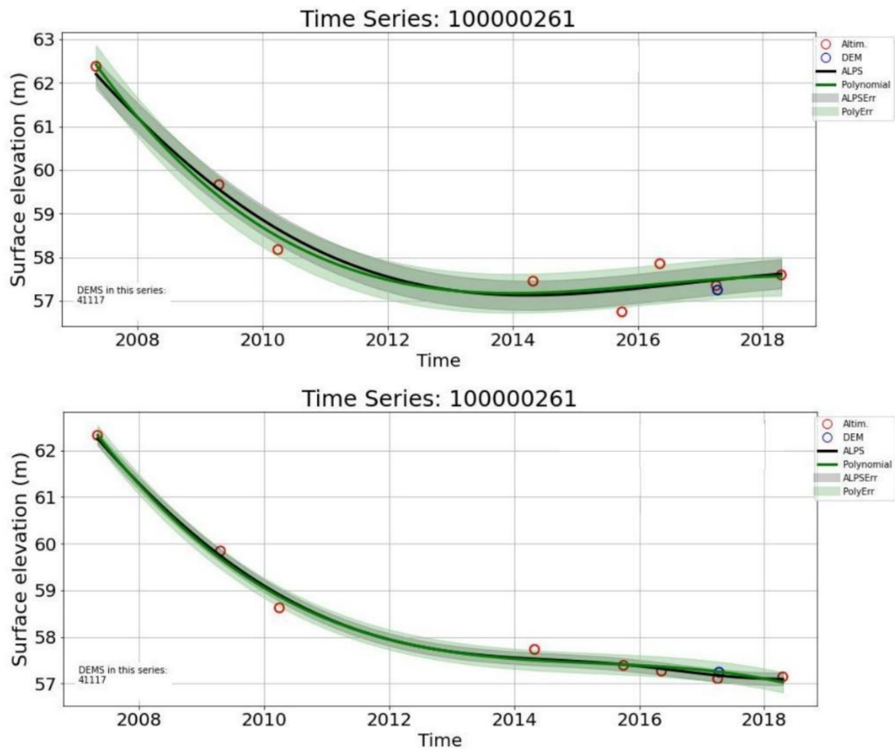

Figure S3. A typical altimetry time series on floating ice before (top) and after (bottom) tidal and barometric corrections are applied.

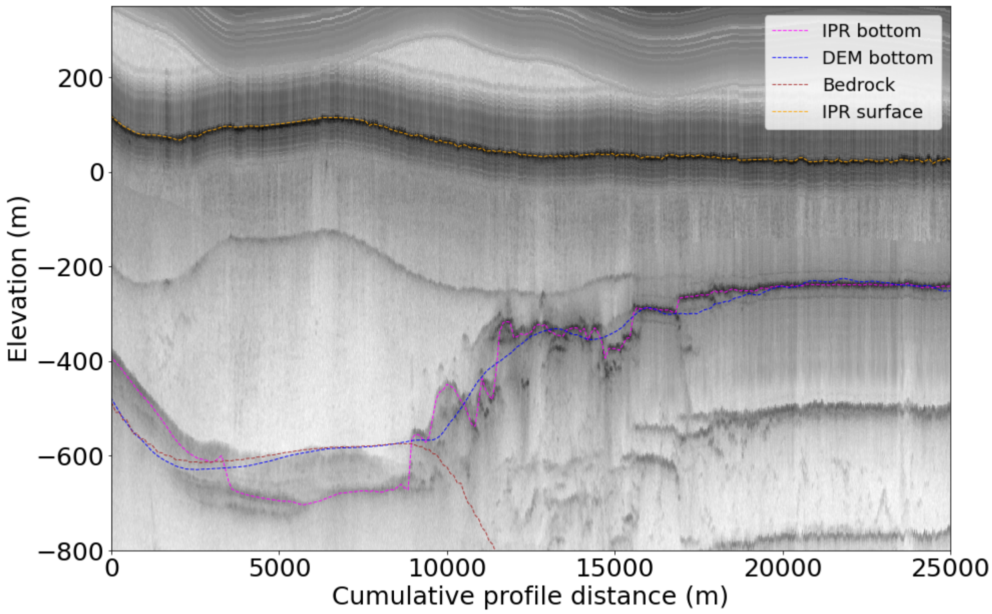

Figure S4. Radar profile from 4/29/2014 (IPR2-IPR2’, Figure 3B) used to estimate the uncertainty of the calculated ice bottom depth.

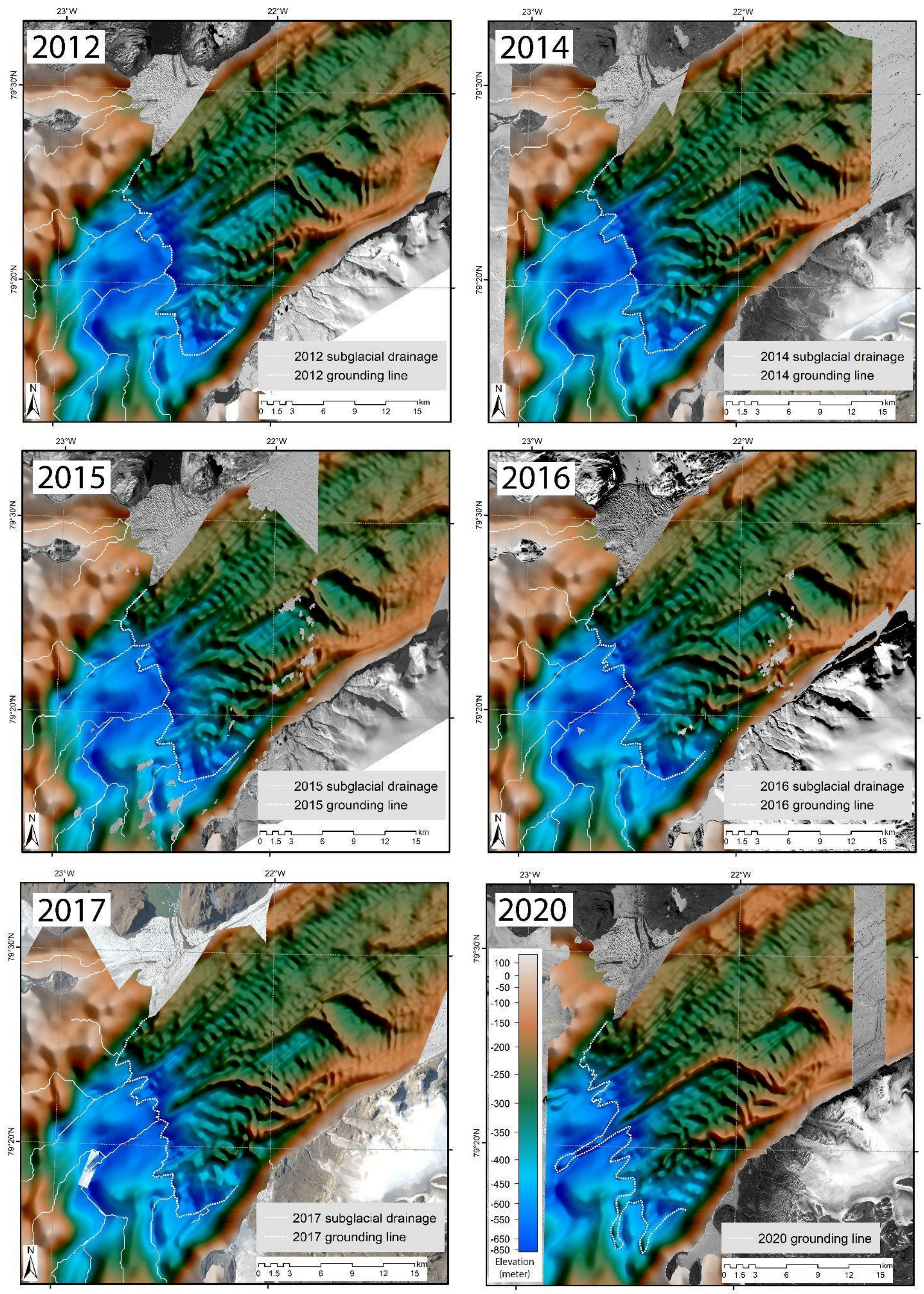

Figure S5. Ice sheet bottom at the grounding zone region in 2012, 2014, 2015, 2016, 2017 and 2020. Elevation of the ice bottom is shown under the floating tongue and bedrock elevation under the grounded ice sheet. All elevations are on the EIGEN-6C4 geoid (a.s.l). Dotted lines are grounding line locations and solid lines are subglacial drainage. Backgrounds are Landsat imagery listed in Table S2.

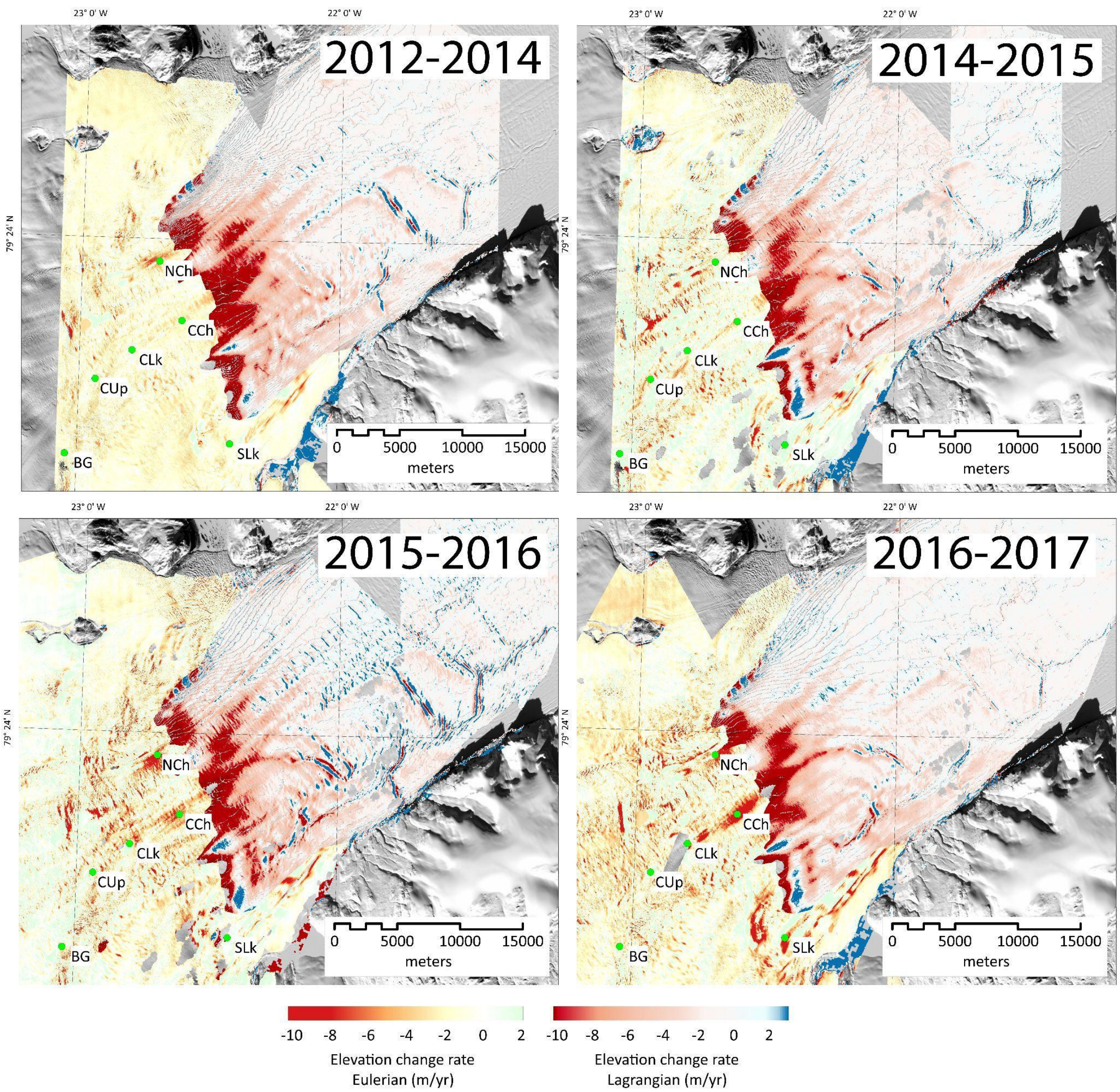

Figure S6. Annual thickness change rates between Spring of 2012-2014, 2014-2015, 2015-2016 and 2016-2017. Eulerian thinning (fixed reference frame) is shown over grounded ice and Lagrangian thinning (moving reference frame) on floating ice.

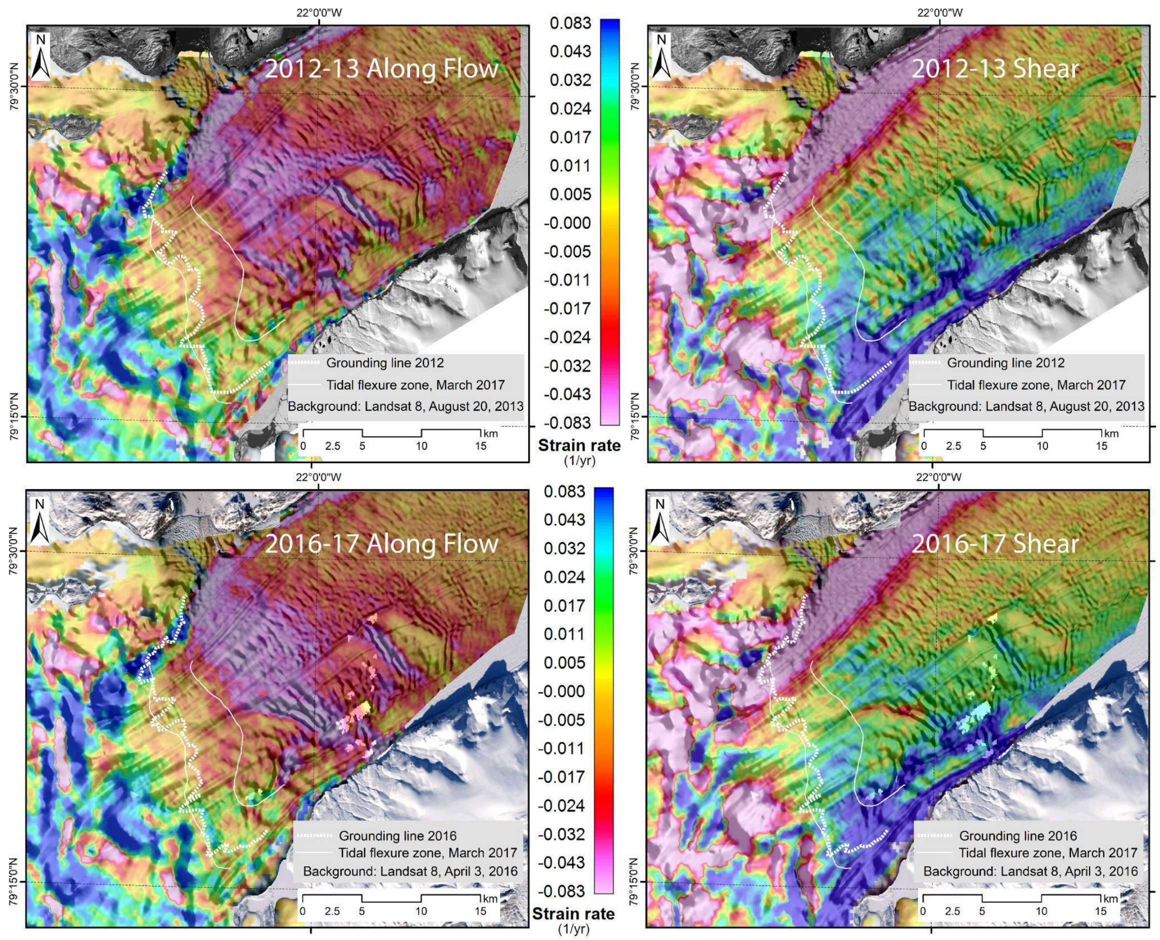

Figure S7. Along- and across- flow strain rate components from annual average velocity overlain in 2012-13 and 2016-17 on shaded relief DEMs. Background is Landsat 8 imagery (Table S2). 2016-17 strain rates are also shown in Figure 4 and included here for easy comparison.

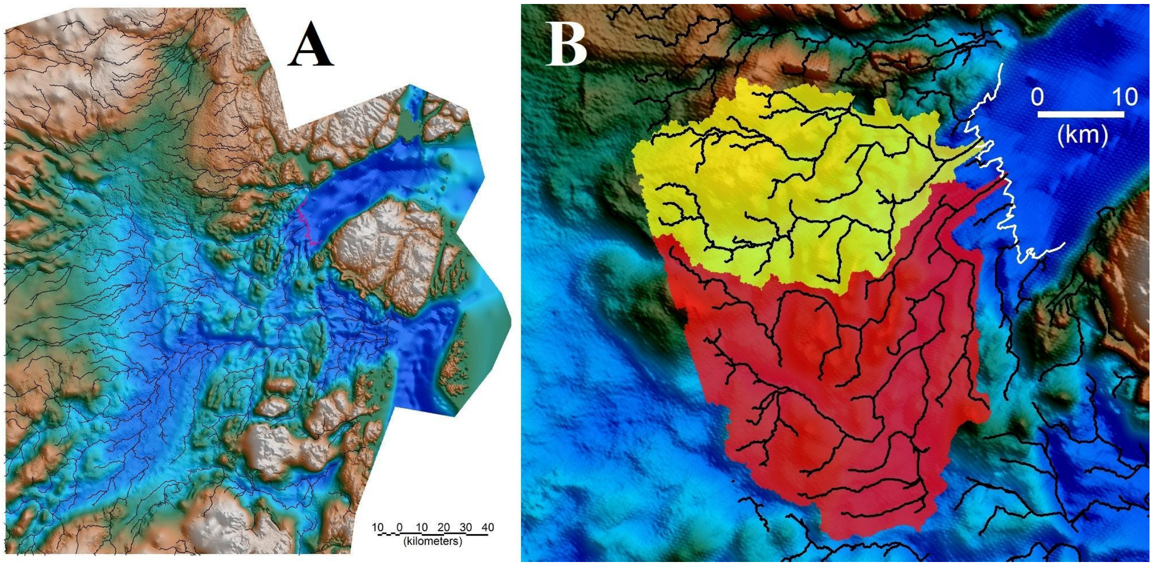

Figure S8. Subglacial routing over bed topography in 2017 (A), with extent of subglacial drainage basin boundaries on grounded ice (B).

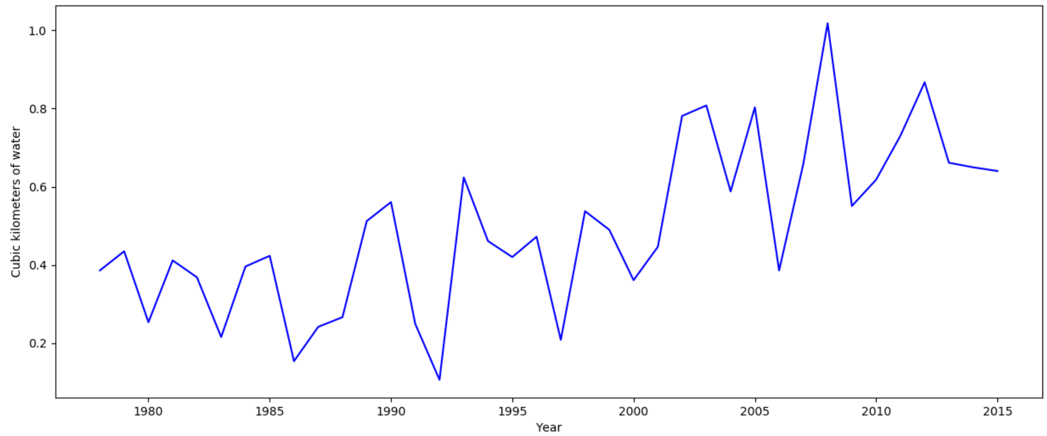

Figure S9. Cumulative runoff within the N79 drainage basin (Fig. S8 red and yellow regions combined) for the years 1978-2016.

Table S1 List of DEMs used for each reconstruction

Table S1A. 2012 Reconstruction, nominal date: 6/12/2012

Mosaic Order	ArcticDEM Filename
1	WV02_20120427_1030010017442400_1030010017B34300_seg1_2m_v3.0
2	WV01_20120430_10200100198A9500_1020010018D64700_seg1_2m_v3.0
3	WV01_20120621_102001001B348A00_102001001AA65A00_seg1_2m_v3.0
4	WV01_20120515_102001001BD59B00_102001001B4BAF00_seg1_2m_v3.0
5	WV01_20120531_102001001B433100_102001001B2D1C00_seg1_2m_v3.0
6	WV01_20120531_102001001B772400_102001001B530900_seg1_2m_v3.0
7	WV01_20120622_102001001C358B00_102001001B849800_seg1_2m_v3.0
8	WV01_20120514_102001001A7F8100_102001001BE40F00_seg1_2m_v3.0
9	WV01_20120805_102001001C9B5A00_102001001A32DB00_seg1_2m_v3.0
10	WV02_20120801_103001001AD82300_103001001A1E1200_seg4_2m_v3.0
11	WV02_20120417_1030010012816700_1030010013109E00_seg1_2m_v3.0

Table SB. 2014 Reconstruction, nominal date: 4/5/2014

Mosaic Order	ArcticDEM Filename
1	WV01_20140405_102001002DC0DF00_102001002CAEC500_seg1_2m_v3.0
2	WV01_20140323_102001002D294100_102001002FA8DD00_seg1_2m_v3.0
3	WV02_20140408_1030010030AA1D00_103001002F63F100_seg1_2m_v3.0
4	WV02_20140323_103001002E792700_103001002F822700_seg1_2m_v3.0
5	WV01_20140427_102001002ED1EA00_102001002D2F1100_seg2_2m_v3.0

Table S1C. 2015 Reconstruction, nominal date: 4/14/2015

Mosaic Order	ArcticDEM Filename
1	WV01_20150406_102001003DD47D00_102001003B1A2900_seg1_2m_v3.0
2	WV02_20150415_1030010041B3DF00_10300100405F0900_seg1_2m_v3.0
3	WV03_20150406_10400100092E6500_104001000A6E9400_seg1_2m_v3.0
4	WV03_20150420_104001000A388800_104001000A155100_seg1_2m_v3.0
5	WV02_20150419_1030010041026D00_1030010041B9F400_seg1_2m_v3.0
6	WV03_20150419_104001000A800900_104001000A064400_seg1_2m_v3.0
7	WV01_20150417_102001003C929A00_102001003B825400_seg1_2m_v3.0

Table S1D. 2016 Reconstruction, nominal date: 3/26/2016

Mosaic Order	ArcticDEM Filename
1	WV03_20160320_104001001ABCA500_104001001A749100_seg1_2m_v3.0
2	WV01_20160404_102001004C2E5000_102001004992DA00_seg1_2m_v3.0
3	W1W1_20160331_102001004992DA00_102001004D8C6D00_seg1_2m_v3.0
4	WV01_20160331_1020010050710900_102001004D8C6D00_seg1_2m_v3.0
5	WV02_20160317_1030010054AE2600_103001005327A800_seg1_2m_v3.0
6	WV02_20160320_103001005341D700_1030010052688600_seg1_2m_v3.0
7	WV03_20160321_104001001994D300_1040010019BC8700_seg1_2m_v3.0
8	WV02_20160323_103001005314A300_1030010053A89300_seg1_2m_v3.0

Table S1E. 2017 Reconstruction, nominal date: 3/27/2017

Mosaic Order	ArcticDEM Filename
1	WV01_20170411_1020010061672400_102001006117A500_seg1_2m_v3.0
2	WV01_20170403_102001005D62FB00_102001005D08D300_seg1_2m_v3.0
3	WV03_20170320_104001002AC32A00_104001002B8CB000_seg1_2m_v3.0
4	WV02_20170317_10300100660BAA00_10300100650DD100_seg1_2m_v3.0
5	WV03_20170327_104001002A23AD00_10400100296CB400_seg1_2m_v3.0
6	WV03_20170326_104001002B0F7700_104001002B29B500_seg1_2m_v3.0
7	WV03_20170326_104001002A6FB700_104001002A69F800_seg1_2m_v3.0
8	WV01_20170330_102001005E45E900_102001005A66CE00_seg1_2m_v3.0

Table S1F. 2020 Reconstruction, nominal date: 6/5/2020

Mosaic Order	ArcticDEM Filename
1	SETSM_s2s041_WV02_20200927_10300100AD1B3600_10300100B07B9D00_2m_lsf_seg1
2	SETSM_s2s041_WV02_20200820_10300100AB446100_10300100AC7C1F00_2m_lsf_seg1
3	SETSM_s2s041_WV03_20200328_104001005838AF00_104001005947AB00_2m_lsf_seg1
4	SETSM_s2s041_WV02_20200324_10300100A5145500_10300100A2381A00_2m_lsf_seg1
5	SETSM_s2s041_WV02_20200406_10300100A3776100_10300100A5C08300_2m_lsf_seg1
6	SETSM_s2s041_WV02_20200717_10300100A9337000_10300100AC499B00_2m_lsf_seg1
7	SETSM_s2s041_WV03_20200917_104001005E73FF00_104001005F2F4A00_2m_lsf_seg1
8	SETSM_s2s041_WV02_20200824_10300100AAD28400_10300100AC8E6B00_2m_lsf_seg8

Table S2 List of aerial and satellite images used as figure backgrounds

Date	Sensor	Full ID Name	Figures
Jul 3, 1978	Aerial camera	g150_1978_utm27_1&2 (orthophotographs)	1D, S1A, S1B
Aug 20, 2013	Landsat 8	LC08_L1TP_014002_20130820_20170502_01_T1_B8	S1, S5, S7
Aug 24, 2013	Landsat 8	LC08_L1TP_010002_20130824_20200912_02_T1_B8	S1
Aug 24, 2013	Landsat 8	LC08_L1TP_010002_20130824_20200913_02_T1_B8	S1
Sep 8, 2014	Landsat 8	LC08_L1TP_014002_20140908_20170419_01_T1_B8	S5
Sep 11, 2015	Landsat 8	LC08_L1TP_014002_20150911_20170404_01_T1_B8	S5
Apr 3, 2016	Landsat 8	LC08_L2SP_009003_20160403_20200907_02_T1_B4	4, S5, S7
Mar 30, 2017	Landsat 8	LC08_L2SP_008003_20170330_20200904_02_T1_B4	2, 3, S6
Aug 3, 2017	Landsat 8	LC08_L1TP_010003_20170803_20200903_02_T1_B4,3,2	1A, 1B, 1E, S5
Jun 29, 2020	Landsat 8	LC08_L1TP_013002_20200629_20200708_01_T1_B8	1F, S5

Supplemental Bibliography

Foerste, C., Bruinsma, S. L., Abrykosov, O., Lemoine, J.-M., Marty, J. C., Flechtner, F., Balmino, G., Barthelmes, F., Biancale, R. (2014). EIGEN-6C4 The latest combined global gravity field model including GOCE data up to degree and order 2190 of GFZ Potsdam and GRGS Toulouse. *GFZ Data Services.* https://doi.org/10.5880/icgem.2015.1

Padman, L., Siegfried, M. R., & Fricker, H. A. (2018). Ocean tide influences on the Antarctic and Greenland ice sheets. *Reviews of Geophysics*, 56, 142–184. doi: 10.1002/2016RG000546

Sutterley, T. C., Markus, T., Neumann, T. A., van den Broeke, M., van Wessem, J. M., Ligtenberg, S. R. M. (2019) Antarctic ice shelf thickness change from multimission lidar mapping. *The Cryosphere,* 13(7), 1801–1817. doi: 10.5194/tc-13-1801-2019